DRIVING MUTUALLY COUPLED COILS USING AN ARRAY OF CLASS-E AMPLIFIERS

A THESIS SUBMITTED TO

THE GRADUATE SCHOOL OF ENGINEERING AND SCIENCE

OF BILKENT UNIVERSITY

IN PARTIAL FULFILLMENT OF THE REQUIREMENTS FOR

THE DEGREE OF

MASTER OF SCIENCE

IN

ELECTRICAL AND ELECTRONICS ENGINEERING

By

Ziba Arghiani

September 2022

DRIVING MUTUALLY COUPLED COILS USING AN ARRAY OF CLASS-E AMPLIFIERS
By Ziba Arghiani
September 2022

We certify that we have read this thesis and that in our opinion it is fully adequate, in scope and in quality, as a thesis for the degree of Master of Science.

Ergin Atalar(Advisor)

Abdullah Atalar

Barış Bayram

Approved for the Graduate School of Engineering and Science:

Orhan Arıkan
Director of the Graduate School

ABSTRACT

DRIVING MUTUALLY COUPLED COILS USING AN ARRAY OF CLASS-E AMPLIFIERS

Ziba Arghiani
M.S. in Electrical and Electronics Engineering
Advisor: Ergin Atalar
September 2022

Linear radiofrequency (RF) power amplifiers are commonly used in magnetic resonance imaging (MRI) to generate radiofrequency field (B_1). These low-efficiency amplifiers require cooling systems and lengthy transmission cabling, increasing the MRI hardware cost. An array of on-coil class-E amplifiers is proposed for the transmit system to mitigate these problems. Class-E amplifiers are switching type amplifiers capable of achieving 100% power efficiency theoretically. In this dissertation, a state-space model is proposed to simplify interpreting and analysis, and provide insight into the system of on-coil class-E amplifiers. This model can also be employed to find high power and efficiency modes of amplifiers' operation. Using the state-space model, phase delays are adjusted between gate signals of the amplifiers to obtain high power and efficiency even in the presence of highly coupled coils. In addition, a sampled-data system generated from the state-space model is proposed to analyze the system's transient behavior by investigating the time constant of the system. To validate the state-space model, a single class-E amplifier and two class-E amplifiers with coupled coils are simulated in LTSPICE. Moreover, novel hardware is designed for the class-E amplifier resulting in a cost-efficient design. Simulation and experimental results are provided to demonstrate the effectiveness of the proposed model.

Keywords: MRI system, state-space model, class-E amplifier, transmit array system.

ÖZET

E-SINIFI YÜKSELTEÇ DİZİSİ KULLANARAK KUPLAJLI BOBİNLERİN SÜRÜLMESİ

Ziba Arghiani
Elektrik ve Elektronik Mühendisliği, Yüksek Lisans
Tez Danışmanı: Ergin Atalar
Eylül 2022

Manyetik rezonans görüntülemede (MRG) lineer radyo frekans (RF) güç yükselteçleri RF manyetik alanı (B_1) oluşturmak için yaygın olarak kullanılır. Verimliliği düşük olan lineer yükselteçler soğutma sistemleri ve uzun iletim kabloları gerektirir ve bu da MRG donanım maliyetini artırır. Verici sistemde bu sorunları azaltmak için bir dizi bobin üzerinde E-sınıfı yükselteçler önerilmiştir. E-sınıfı güç yükselteçleri teorik olarak 100% güç verimliliği elde edebilen anahtarlamalı tip bir amplifikatördür. Bu tezde, yorumlamayı ve analizi basitleştirerek ve bobin-üstü E-sınıfı yükselteç dizileri hakkında bilgi sağlamak için bir durum-uzay modeli önerilmiştir. Bu model ayrıca yükselteçlerin çalışmasında yüksek güç ve verimlilik modlarını bulmak için kullanılabilir. Durum-uzay modeli kullanılarak yüksek düzeyde etkileşim gösteren bobinlerin varlığında bile yüksek güç ve verimlilik elde etmek için yükselteçlerin kapı sinyalleri arasındaki faz gecikmeleri ayarlanır. Ek olarak durum-uzay modelinden yola çıkarak elde edilen örneklenmiş veriler sistemin ani değişimler karşısındaki tepki hızını göstermiştir. Durum-uzay modelini doğrulamak için, LTSPICE'ta tek bir E-sınıfı yükselteç ve birleştirilmiş bobinlere sahip iki E-sınıfı yükselteç simüle edilmiştir. Ayrıca E-sınıfı yükselteç için yeni ve daha uygun maliyetli bir donanım tasarlanmıştır. Önerilen modelin etkinliğini göstermek için simülasyon ve deneysel sonuçlar sağlanmıştır.

Anahtar sözcükler: MRI sistemi, durum-uzay modeli, E-sınıfı yükselteç, verici dizisi sistemi.

Acknowledgement

I would like to thank the following people, without whom I would not have been able to complete this research. First and foremost I am extremely grateful to my supervisor, Prof. Ergin Atalar for his invaluable advice, continuous support, an patience during my MSc study. His immense knowledge and plentiful experience have encouraged me in all the time of my academic research and daily life. It is my honor to have Prof. Abdullah Atalar and Prof. Barış Bayram in my dissertation committee and I would like to thank them for their invaluable comments and questions about my thesis. I would like to thank Dr. Manouchehr Takrimi for his technical support on my study. I would also like to thank all the members in the Ergin Atalar laboratory, Said Aldemir, Reza Babaloo, Abdullah Erkam Arslan, Ehsan Kazemivalipour, Alireza Sadeghi-Tarakameh, Soheil Taraghinia, Fatma Gul Uyar, Mehmet Tilegi, Bilal Tasdelen, Cemre Ariyurek and Elnaz Mahmoudi Mahmoud Alilou. It is their kind help and support that have made my study and life in Bilkent a wonderful time. I would like to express my gratitude to my family. Without their tremendous understanding and encouragement in the past few years, it would be impossible for me to complete my study. Finally, I owe my deepest gratitude to Shahab, who is my love. I am forever thankful for the unconditional love and support throughout the entire thesis process and every day.

Contents

List of Figures

List of Tables

Chapter 1

Introduction

Magnetic resonance imaging (MRI) is a non-invasive and non-destructive technique for imaging the internal structures and specific aspects of function within the body [1, 2]. MRI scanners consist of a magnet, which provides a powerful static magnetic field (B_0) that forces protons in the body to align with its direction, gradient, and radiofrequency (RF) systems [3, 4]. The gradient system, including gradient amplifiers and coils, generates three gradient fields, orthogonal to each other, for spatial encoding within an imaging volume [4, 5]. The radiofrequency (RF) system consists of an RF power amplifier and transmit and receive coils. The power amplifier provides RF pulses for the RF coils, which generate RF magnetic field (B_1) to excite the aligned spins and receive an RF signal back from the target [6, 7, 8, 9].

In conventional MRI systems, linear RF power amplifiers are commonly employed. The efficiency of these amplifiers is relatively low. Therefore, a bulky cooling system is needed to cool them down. They are required to be located in the MRI system room, far from the transmit coils in the MRI scanner. The requirement for long transmission cables between the amplifier and the RF coils leads to additional power loss. The above-mentioned problems result in a more expensive and complex system with low efficiency [10, 11].

Radiofrequency coils are essential to MRI systems. These coils that excite and receive MRI signals can be designed as transmit-only (Tx), receive-only (Rx), and transmit/receive (Tx/Rx) coils [12, 13]. Volume coils, such as birdcage coils, are typically used as transmit coils to achieve a homogeneous RF excitation (B_1) field for the entire covered volume [9]. In ultra high-field MRI systems (>3T), birdcage coils can not provide a uniform and homogeneous B_1 field due to the shorter wavelength and standing wave effect [13, 14]. It is investigated in [15] that parallel excitation with an array of transmit coils can enhance the transmit field (B_1) inhomogeneity at ultra high fields [16], leading to more accurate excitation. Transmit array technology is proved to be useful in systems with conventional field strengths such as 1.5 and 3T. Parallel excitation using transmit (Tx) arrays improves RF excitation, becoming multidimensional and spatially selective RF excitation [17]. This method also shortens selective RF pulses in two or three dimensions, minimizes local specific absorption rate (SAR), and achieves the extra degrees of freedom of the system [17]. Moreover, this method allows independent control of the phase and amplitude of transmit coil elements [15].

Several studies are conducted to implement TxArray systems [18, 19]. For example, in the work presented in [20], the efficient modes of operation of TxArray coils are investigated by applying an eigenmode analysis of the scattering matrix. Implementing these TxArray systems becomes complicated as the number of elements increases. For instance, controlling and supplying multiple linear power amplifiers need more cabling and high cost. Furthermore, using multiple power radio frequency (RF) cables leads to cable coupling and mechanical stress, which needs to be considered. Also, tuning, matching, and decoupling the arrays' elements become more complex [21]. Therefore, considering these issues, some different RF amplifier designs are proposed for TxArrays [22, 23].

As a novel idea to tackle linear RF power amplifiers' problems, high efficient on-coil amplifiers are employed [11, 21, 16, 24]. Recently, in work by Gudino [25], an eight-channel parallel transmit-receive system is implemented with optimized on-coil current mode class-D amplifiers. These amplifiers can deliver more than 100W power and provide enough amplifier decoupling (less than -15dB) in the system.

Class-E amplifiers are switching type amplifiers capable of achieving 100% power efficiency theoretically. The amplifier can reach the highest efficiency when two conditions of zero-voltage switching (ZVS) and zero-voltage derivative switching (ZVDS) are achieved. It consists of a choke inductor, a shunt capacitor, and an RLC load network [26]. This amplifier was initially presented by Sokal, and Sokal [27]. In our research group in UMRAM, class-E amplifiers have been proposed as on-coil amplifiers for MRI transmit array systems. Poni designed a modified class-E amplifier for 3T that was digitally controlled, with 100W power and efficiency up to 88% [28]. In his design, the transmit coil is considered as the RLC network. Therefore, matching is not required at 50Ω in both coil and amplifier sides. Zahra implemented a class-E RF amplifier with supply modulation with an output power of 300W and maximum power efficiency of 92% [29]. In work by Ashfaq [30], a novel technique for gate modulation of modified class-E amplifiers is proposed. Optimizing coupled class-E power amplifiers for a transmit array system in 1.5T is also presented by Aldemir [10]. The author of [10] proposed the state-space model of an ideal class-E amplifier. Then the model is applied to two class-E amplifiers with coupled coils to optimize the circuits' parameters for high power and efficiency in the system. A 600W on-coil class-E RF power amplifier array with dynamic phase control is presented for 3T MRI by Erkam Arslan [31].

This thesis proposes a state-space model for an array of on-coil class-E amplifiers considering switches' on-resistance and coupling effects between the coils. Using this model and applying phase delays between the gate signals of the amplifiers, modes of the system associated with high power and efficiency can be found. The sampled-data system generated from the state-space model equips the designer with a powerful tool for analyzing the transient behavior by investigating the efficiency and time constant. In addition, novel hardware is also designed for the class-E amplifier. In this design, the goal is to retain high efficiency while reducing the size of the PCB and price.

The main motivation of this work is to find a model that can enable us to investigate and analyze an array of on-coil class-E amplifiers in the presence of coupling between coils. In order to deliver more power, it is required to increase the number of on-coil amplifiers, and consequently, the coupling between coils becomes problematic. This causes power and efficiency reduction in the system. There are some methods, such as adding decoupling circuits to eliminate coupling effects. In this work, using the state-space model, it is shown that the system can reach high power and efficiency even in the presence of high coupling between coils. This is done by adding proper phase delays between the gate signals of the amplifiers. In addition, the proposed state-space model provides a comprehensive insight into the system even with a high number of channels. Also, a sampled data system is derived from this state-space model, which provides a tool for analyzing the system's transient behavior.

This thesis is organized as follows. Chapter 2 introduces a state-space model for an array of class-E amplifiers considering the coupling effects between coils. Then, the steady-state solution of the system is explained in detail, and transient analysis is proposed for the system. Chapter 3 presents the methods for analyzing the behavior of a class-E amplifier and an array of class-E amplifiers with coupled coils. The hardware design, simulations, implementation, and lab experiments are also explained in this chapter. Simulation results of the state-space model of a single class-E amplifier, two and three class-E amplifiers with significantly coupled coils are presented in chapter 4. This chapter also compares the experimental and simulation results of the designed amplifier. Finally, in chapter 5, a summary of the proposed methods is provided, and future works are discussed.

Chapter 2

Theory

This chapter presents a state-space model for a class-E power amplifier using differential equations for capacitors' voltages and inductors' currents. Class-E amplifier is a switching type amplifier, and a gate driver signal turns on and off the amplifier's switch periodically. Since this switch is not ideal, its on-resistance is also considered when deriving the equations. Then, the steady-state solution of the proposed model is obtained to analyze the amplifier's behavior. This is done by finding the steady-state waveforms, input and output powers, and power efficiency. The state-space model is also developed for an array of class-E amplifiers while there is coupling between its inductive loads. Using this model, the whole system's behavior can be analyzed, and similarly, the powers and efficiency can be calculated for each amplifier and the system. A sampled-data system is introduced using the state equations at each period. This sampled-data system can be used to analyze the transient behavior of the system and find prominent information about the system, like time constant. Finally, a new design for the class-E amplifier's circuit is proposed, which includes driver and supply modulation. Since the amplifier can be controlled digitally, a driver circuit is designed to provide enough current and voltage levels to the gate of MOSFET. In addition, to improve efficiency, a supply modulation circuit is also designed for envelope control.

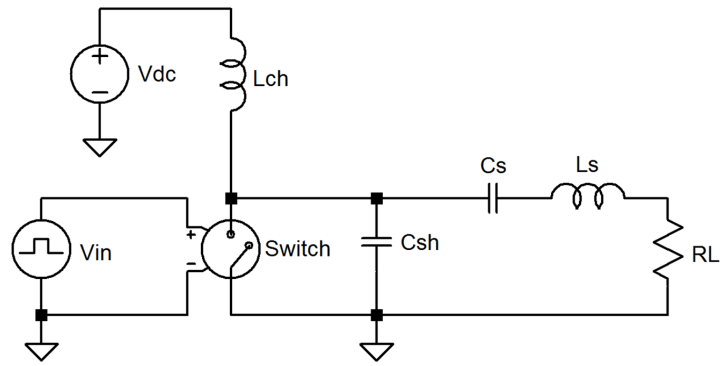

Figure 2.1: Conventional class-E amplifier circuit

2.1 Conventional Class-E Amplifier

A class-E power amplifier is a non-linear and switching amplifier with a theoretical 100% drain efficiency. As illustrated in Fig. 2.1, the class-E amplifier consists of a switch which is a transistor typically, a shunt capacitor (C_{sh}), a choke inductor (L_{ch}), a supply voltage (V_{dc}), and a load network which includes a series resonator (L_s-C_s) and a load resistor (R_L).

The choke inductor is used to supply a DC current between the voltage source and the switch while blocking the RF signal. To achieve 100% efficiency from the class-E amplifier, two conditions of zero-voltage switching (ZVS) and zero-voltage derivative switching (ZVDS) should be satisfied by tuning the load network and adjusting the parallel capacitor value at the same time. In addition, it is also assumed that the switch is ideal and all capacitors and inductors are lossless. The input signal, a square wave, controls the switch's condition. In this case, a sinusoidal RF current flows across the load resistor (R_L) by considering that the series resonator circuit's quality factor (Q) is high enough.

Figure 2.2 shows the switch voltage and current waveforms. As can be seen in this figure, when the switch is off for the first half of the period, the switch's voltage is non-zero, and its current is zero. Similarly, when the switch is turned on for the second half of the period, the current only flows through the switch,

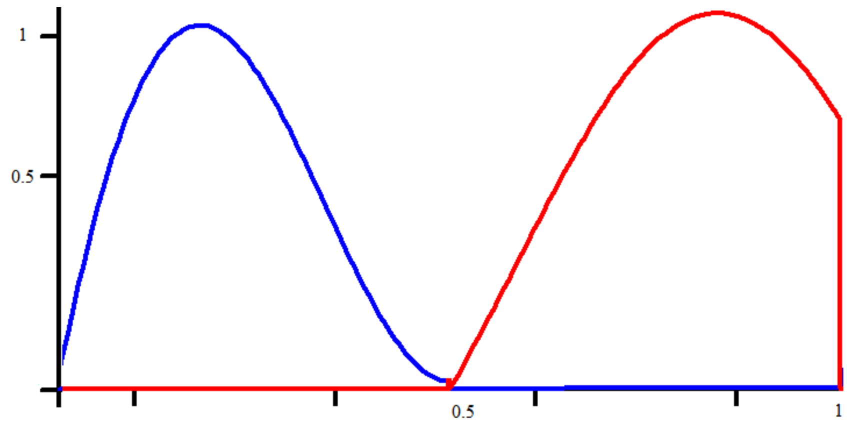

Figure 2.2: Normalized voltage (blue) and current (red) of the switch of a class-E amplifier versus normalized time

and the voltage across it is zero.

The following equations explain the operation principles of a class-E amplifier [32]. The switch is off in the first half of the period, and its current is zero. Therefore, the current and voltage of the shunt capacitor can be found as

$$i_{C_{sh}} = I_{L_{ch}} - i_{R_L}, \tag{2.1}$$

$$C_{sh}\frac{dV_{C_{sh}}(t)}{dt} = I_{L_{ch}} - i_{R_L}. \tag{2.2}$$

Assuming that the load current is a sinusoidal signal, it can be written as

$$i_{R_L}(t) = \alpha I_{L_{ch}} \sin(\omega_s t + \phi), \tag{2.3}$$

where ω_s and ϕ are the fundamental frequency and the phase shift respectively. Therefore, the voltage of shunt capacitor can be found:

$$V_{C_{sh}} = V_{SW} = \frac{I_{L_{ch}}}{\omega_s C_{s_h}}(\omega_s t + \alpha(\cos(\omega_s t + \phi) - \cos(\phi))). \tag{2.4}$$

In order to find maximum efficiency for class-E amplifier the ZVS and ZDVS conditions should be applied.

$$V_{SW}(t)\Big|_{t=\frac{T}{2}} = 0 \tag{2.5}$$

$$\frac{dV_{SW}(t)}{dt}\Big|_{t=\frac{T}{2}} = 0 \tag{2.6}$$

After considering the boundary conditions, α and ϕ are calculated as below:

$$\alpha = 1.86 \quad ; \quad \phi = -32.5^\circ \tag{2.7}$$

By solving the above equations, the voltage and current of the switch can be found for both on and off cases, Eq. 2.8-2.9.

$$V_{SW} = \begin{cases} \frac{I_{L_{ch}}}{\omega_s C_{s_h}}(\omega_s t + \alpha(\cos(\omega_s t + \phi) - \cos(\phi))) & 0 \leq \omega_s t \leq \pi \\ 0 & \pi \leq \omega_s t \leq 2\pi \end{cases} \tag{2.8}$$

$$I_{SW} = \begin{cases} 0 & 0 \leq \omega_s t \leq \pi \\ I_{L_{ch}}(1 - \alpha \sin(\omega_s + \phi)) & \pi \leq \omega_s t \leq 2\pi \end{cases} \tag{2.9}$$

In the implementation of the amplifiers, non-idealities occur. If only the on-resistance is considered, the power loss in the switch and the amplifier efficiency can be found as follows [33]:

$$P_{Rdson} = 1.37\frac{R_{dson}}{R_L}P_{out}, \tag{2.10}$$

$$\eta = \frac{R_L}{R_L + 1.37R_{dson}}100\% \tag{2.11}$$

2.2 State-Space Model of a Class-E Amplifier

The state-space model of an ideal class-E power amplifier has been proposed in the previous work by Aldemir [10]. Since an actual switch, like a MOSFET is not ideal and has a low-on resistance, there will be voltage drop and power loss across it when it is on. Furthermore, it is important to analyze the transient behavior of the amplifier. To develop the previous model for the circuit shown in Fig. 2.1, the switch is assumed to have a small turn-on resistance (R_{dson}) while the differential equations of the system are derived (see Fig. 2.3). The state variables of the system are inductors' currents and capacitors' voltages that are

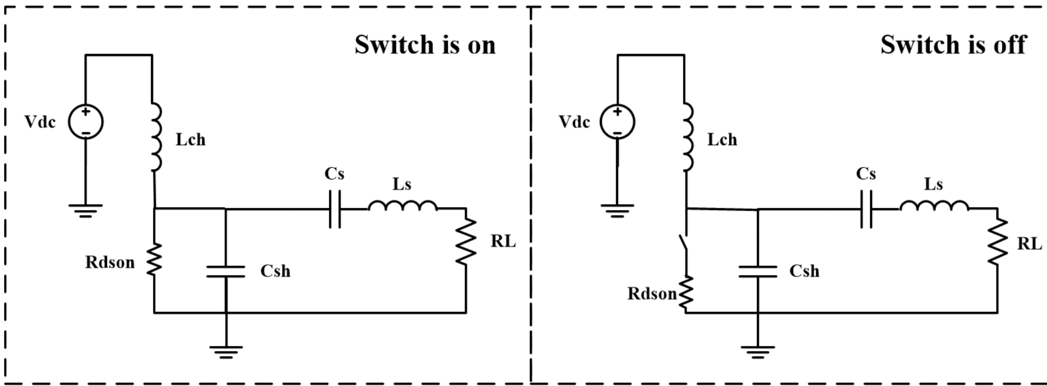

Figure 2.3: Schematic of a class-E amplifier considering switch's on-resistance, R_{dson}

given in Eq. 2.12.

$$\bar{x}(t) = \begin{bmatrix} V_{C_s}(t) \\ I_{L_{ch}}(t) \\ V_{C_{sh}}(t) \\ I_{L_s}(t) \end{bmatrix} \tag{2.12}$$

The state-space model of the system can be expressed by a set of first-order non-homogeneous differential equations for a a single period as below:

$$\frac{d\bar{x}(t)}{dt} = \begin{cases} \bar{\bar{A}}_{on}\bar{x}(t) + \bar{b}_{on} & 0 \leq t \leq t_1, \\ \bar{\bar{A}}_{off}\bar{x}(t) + \bar{b}_{off} & t_1 \leq t \leq T, \end{cases} \tag{2.13}$$

where t_1 determines the switch's on time and it depends on the duty cycle and

$$\bar{\bar{A}}_{on} = \begin{bmatrix} 0 & 0 & 0 & \frac{1}{C_s} \\ 0 & 0 & -\frac{1}{L_{ch}} & 0 \\ 0 & \frac{1}{C_{sh}} & -\frac{1}{R_{dson}C_{sh}} & -\frac{1}{C_{sh}} \\ -\frac{1}{L_s} & 0 & \frac{1}{L_s} & -\frac{R_L}{L_s} \end{bmatrix}, \quad \bar{b}_{on} = \begin{bmatrix} 0 \\ \frac{V_{dc}}{L_{ch}} \\ 0 \\ 0 \end{bmatrix}, \tag{2.14}$$

$$\bar{\bar{A}}_{off} = \begin{bmatrix} 0 & 0 & 0 & \frac{1}{C_s} \\ 0 & 0 & -\frac{1}{L_{ch}} & 0 \\ 0 & \frac{1}{C_{sh}} & 0 & -\frac{1}{C_{sh}} \\ -\frac{1}{L_s} & 0 & \frac{1}{L_s} & -\frac{R_L}{L_s} \end{bmatrix}, \quad \bar{b}_{off} = \begin{bmatrix} 0 \\ \frac{V_{dc}}{L_{ch}} \\ 0 \\ 0 \end{bmatrix}, \tag{2.15}$$

$$\bar{b}_{on} = \bar{b}_{off} = \bar{b}, \tag{2.16}$$

and where $\bar{\bar{A}}_{on}$ and $\bar{b}_{on}$ represent the state matrix and the input vector for "on" state respectively. Similarly, $\bar{\bar{A}}_{off}$ and $\bar{b}_{off}$ explain "off" state. The input vectors are the same for both states, Eq. 2.16. In the steady state condition, the solution of Eq. 2.13 is as follows:

$$\bar{x}(t) = \begin{cases} \bar{x}_{on}(t) \equiv e^{\bar{\bar{A}}_{on}t}\bar{x}(0) + \bar{\bar{A}}_{on}^{-1}(e^{\bar{\bar{A}}_{on}t} - I)\bar{b} & 0 \leq t \leq t_1, \\ \bar{x}_{off}(t) \equiv e^{\bar{\bar{A}}_{off}(t-t_1)}\bar{x}(t_1) + \bar{\bar{A}}_{off}^{-1}(e^{\bar{\bar{A}}_{off}(t-t_1)} - I)\bar{b} & t_1 \leq t \leq T, \end{cases} \tag{2.17}$$

where $x(0)$ and $x(\frac{T}{2})$ are initial conditions for on and off states respectively and $e^{\bar{\bar{A}}t}$ is the matrix exponential of A given by Eq. 2.18.

$$e^{\bar{\bar{A}}t} = \sum_{n=1}^{\infty} \frac{t^n}{n!}\bar{\bar{A}}^n = I + \frac{t}{1!}\bar{\bar{A}} + \frac{t^2}{2!}\bar{\bar{A}}^2 + \frac{t^3}{3!}\bar{\bar{A}}^3 + ... + \frac{t^k}{k!}\bar{\bar{A}}^k + ... \tag{2.18}$$

To simplify the expressions, the following notations are applied:

$$\bar{\bar{F}}_{on}(t) = e^{\bar{\bar{A}}_{on}t}, \quad \bar{q}_{on}(t) = \bar{\bar{A}}_{on}^{-1}(e^{\bar{\bar{A}}_{on}t} - I)\bar{b}, \tag{2.19}$$

$$\bar{\bar{F}}_{off}(t) = e^{\bar{\bar{A}}_{off}(t-t_1)}, \quad \bar{q}_{off}(t) = \bar{\bar{A}}_{off}^{-1}(e^{\bar{\bar{A}}_{off}(t-t_1)} - I)\bar{b}. \tag{2.20}$$

After the amplifier reaches the steady-state, the waveforms repeat at switching frequency. In this case, the final value of state vector at each time interval should be chosen as the initial condition for the next time interval as follows:

$$\bar{x}(0) = \bar{x}_{on}(0) = \bar{x}_{off}(T) = \bar{\bar{F}}_{off}(T)\bar{x}(t_1) + \bar{q}_{off}(T), \tag{2.21}$$

$$\bar{x}(t_1) = \bar{x}_{on}(t_1) = \bar{x}_{off}(t_1) = \bar{\bar{F}}_{on}(t_1)\bar{x}(0) + \bar{q}_{on}(t_1). \tag{2.22}$$

By solving Eq. 2.21 and Eq. 2.22, $\bar{x}(0)$ and $\bar{x}(\frac{T}{2})$ can be found as:

$$\bar{x}(0) = \left(I - \bar{\bar{F}}_{off}(T)\bar{\bar{F}}_{on}(t_1)\right)^{-1}\left(\bar{\bar{F}}_{off}(T)\bar{q}_{on}(t_1) + \bar{q}_{off}(T)\right), \tag{2.23}$$

$$\bar{x}(t_1) = \left(I - \bar{\bar{F}}_{on}(t_1)\bar{\bar{F}}_{off}(T)\right)^{-1}\left(\bar{\bar{F}}_{on}(t_1)\bar{q}_{off}(T) + \bar{q}_{on}(t_1)\right). \tag{2.24}$$

After initial values of the state vector are determined, the differential equations which represent the behavior of the circuit can be solved in MATLAB for the steady-sate condition. This model enables to simulate and analyze the circuit in different ways such as plotting the waveforms, efficiency and power measurements, tuning capacitors of the amplifier by swiping the circuit parameters, and etc. In addition, it has lower computational burden compared to the existing circuit simulators.

Power loss in the amplifier happens for two following reasons. First, since the switch is not ideal, there is a power loss due to its on-resistance. Second, when the two conditions of ZVS and ZVDS are not satisfied, the shunt capacitor may contain a nonzero charge while the switch is turning on. Therefore, the shunt capacitor discharges through the switch, leading to a power dissipation independent of the switch's on-resistance value. The input and output powers and efficiency of a single class-E amplifier are computed over a period using the following equations:

$$P_{R_L} = P_{R_L,on} + P_{R_L,off} = \frac{R_L}{T}\int_{on} I_{L_s}^2(t)\,dt + \frac{R_L}{T}\int_{off} I_{L_s}^2(t)\,dt, \tag{2.25}$$

$$P_{R_L} = \frac{R_L}{T}\int_0^T I_{L_s}^2(t)\,dt, \tag{2.26}$$

$$P_{V_{dc}} = \frac{V_{dc}}{T}\int_0^T I_{L_{ch}}(t)\,dt, \tag{2.27}$$

$$\text{Efficiency} = \eta = \frac{\text{Output RF power}}{\text{Input DC supply power}} = \frac{P_{R_L}}{P_{V_{dc}}}. \tag{2.28}$$

By defining $\bar{e}_{ch} = [0\ 1\ 0\ 0]^T$, $I_{L_{ch}}$ can be written as $I_{L_{ch}} = \bar{e}_{ch}^T\bar{x}$. Thus, we have

$$\begin{aligned} P_{V_{dc}} = \frac{V_{dc}}{T}\int_0^T I_{L_{ch}}(t)\,dt &= \frac{V_{dc}}{T}\int_0^T \bar{e}_{ch}^T\bar{x}(t)\,dt = \frac{V_{dc}}{T}\bar{e}_{ch}^T\int_0^T \bar{x}(t)\,dt \\ &= \frac{V_{dc}}{T}\bar{e}_{ch}^T\left(\int_0^{t_1}\bar{x}(t)\,dt + \int_{t_1}^T \bar{x}(t)\,dt\right). \end{aligned} \tag{2.29}$$

Using Eq. 2.17, Eq. 2.29 can be rewritten as

$$\begin{aligned} P_{V_{dc}} &= \frac{V_{dc}}{T}\bar{e}_{ch}^T\left(\int_0^{t_1}\bar{x}_{on}(t)\,dt + \int_{t_1}^T \bar{x}_{off}(t)\,dt\right) \\ &= \frac{V_{dc}}{T}\bar{e}_{ch}^T(\int_0^{t_1} e^{\bar{\bar{A}}_{on}t}\bar{x}(0) + \bar{\bar{A}}_{on}^{-1}(e^{\bar{\bar{A}}_{on}t} - I)\bar{b}\,dt \\ &+ \int_{t_1}^T e^{\bar{\bar{A}}_{off}(t-t_1)}\bar{x}(t_1) + \bar{\bar{A}}_{off}^{-1}(e^{\bar{\bar{A}}_{off}(t-t_1)} - I)\bar{b}(t)\,dt). \end{aligned} \tag{2.30}$$

By substituting Eq. 2.19, 2.20, and 2.22, Eq. 2.30 can be simplified in terms of $\bar{x}(0)$ as

$$\begin{aligned} P_{V_{dc}} &= \frac{V_{dc}}{T}\bar{e}_{ch}^T\left(\int_0^{t_1}(\bar{\bar{F}}_{on}(t)\bar{x}(0)+\bar{q}_{on}(t))\,dt+\int_{t_1}^{T}(\bar{\bar{F}}_{off}(t)\bar{x}(t_1)+\bar{q}_{off}(t))\,dt\right) \\ &= \frac{V_{dc}}{T}\bar{e}_{ch}^T(\bar{\bar{K}}_1\bar{x}(0)+\bar{K}_2), \end{aligned} \tag{2.31}$$

where

$$\bar{\bar{K}}_1=\int_0^{t_1}\bar{\bar{F}}_{on}(t)\,dt+\int_{t_1}^{T}\bar{\bar{F}}_{off}(t)\bar{\bar{F}}_{on}(t_1)\,dt, \tag{2.32}$$

$$\bar{K}_2=\int_0^{t_1}\bar{q}_{on}(t)\,dt+\int_{t_1}^{T}\bar{\bar{F}}_{off}(t)\bar{q}_{on}(t_1)\,dt+\int_{t_1}^{T}\bar{q}_{off}(t)\,dt. \tag{2.33}$$

It is noted that $\bar{\bar{K}}_1$ and $\bar{K}_2$ are constant matrix and vector, respectively.

By defining $\bar{e}_s=[0\ 0\ 0\ 1]^T$, I_{L_s} can be written as $I_{L_s}=\bar{e}_s^T\bar{x}$, thus we have

$$\begin{aligned} P_{R_L}=\frac{R_L}{T}\int_0^T I_{L_s}^2(t)\,dt &= \frac{R_L}{T}\int_0^T(\bar{e}_s^T\bar{x}(t))^T(\bar{e}_s^T\bar{x}(t))\,dt \\ &= \frac{R_L}{T}\int_0^T\bar{x}^T(t)\bar{e}_s\bar{e}_s^T\bar{x}(t)\,dt. \end{aligned} \tag{2.34}$$

Following a similar procedure for $P_{V_{dc}}$, and using Eq. 2.19, 2.20, and 2.22, Eq. 2.34 can be written in terms of $\bar{x}(0)$ as

$$P_{R_L}=\frac{R_L}{T}\left(\bar{x}^T(0)\bar{\bar{G}}_1\bar{x}(0)+\bar{x}^T(0)\bar{G}_2+\bar{G}_2^T\bar{x}(0)+G_3\right), \tag{2.35}$$

where

$$\bar{\bar{G}}_1=\int_0^{t_1}\bar{\bar{F}}_{on}^T(t)\bar{e}_s\bar{e}_s^T\bar{\bar{F}}_{on}(t)\,dt+\int_{t_1}^{T}\bar{\bar{F}}_{on}^T(t_1)\bar{\bar{F}}_{off}^T(t)\bar{e}_s\bar{e}_s^T\bar{\bar{F}}_{off}(t)\bar{\bar{F}}_{on}(t_1)\,dt, \tag{2.36}$$

$$\bar{G}_2=\int_0^{t_1}\bar{\bar{F}}_{on}^T(t)\bar{e}_s\bar{e}_s^T\bar{q}_{on}(t)\,dt+\int_{t_1}^{T}\bar{\bar{F}}_{on}^T(t_1)\bar{\bar{F}}_{off}^T(t)\bar{e}_s\bar{e}_s^T(\bar{\bar{F}}_{off}(t)\bar{q}_{on}(t_1)+\bar{q}_{off}(t))\,dt, \tag{2.37}$$

$$\begin{aligned} G_3 &= \int_0^{t_1}\bar{q}_{on}^T(t)\bar{e}_s\bar{e}_s^T\bar{q}_{on}(t)\,dt+\int_{t_1}^{T}\bar{q}_{on}^T(t_1)\bar{\bar{F}}_{off}^T(t)\bar{e}_s\bar{e}_s^T\bar{\bar{F}}_{off}(t)\bar{q}_{on}(t_1)\,dt \\ &\quad +2\int_{t_1}^{T}\bar{q}_{on}^T(t_1)\bar{\bar{F}}_{off}^T(t)\bar{e}_s\bar{e}_s^T\bar{q}_{off}(t)\,dt+\int_{t_1}^{T}\bar{q}_{off}^T(t)\bar{e}_s\bar{e}_s^T\bar{q}_{off}(t)\,dt. \end{aligned} \tag{2.38}$$

It is noted that $\bar{\bar{G}}_1$ is a constant matrix, $\bar{G}_2$ is a constant vector, and G_3 is a constant. This implies that the input and output powers (2.26 and 2.27) can be written in terms of initial values of the states, as indicated in Eq. 2.31 and Eq. 2.35.

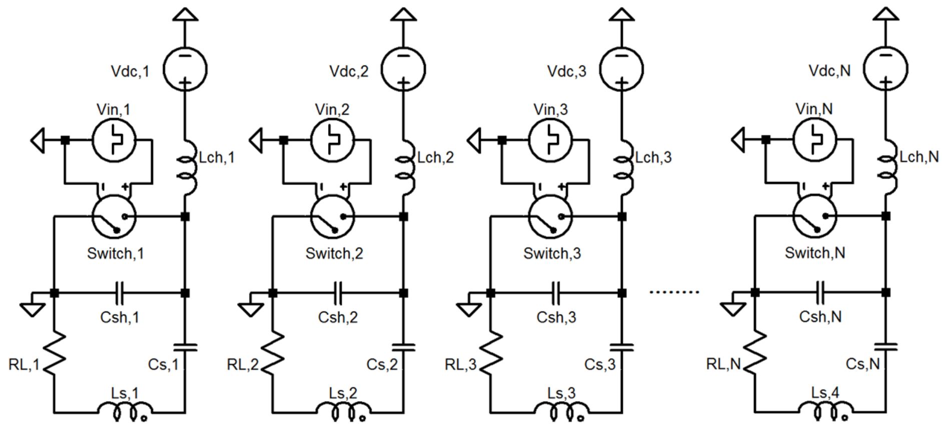

Figure 2.4: An array of class-E amplifiers with coupled loads

2.3 Model of An Array of Class-E Amplifiers with Coupled Load

The state-space model for a single channel class-E amplifier has been introduced in the previous section. In a real MRI scanner, multi-channel class-E amplifiers are required to achieve highest output power. When the number of amplifiers are increased, the inductive coupling between amplifiers may affect output power and efficiency of the system. In order to understand the behavior of such a system and analyze it, the state-space model is developed for an array of coupled class-E amplifiers as shown in Fig. 2.4.

Since each amplifier has 4 storage elements (2 capacitors and 2 inductors), the total number of state variables is $4 \times N$. The state vector of the the system is defined as follows:

$$\bar{x}(t) = \begin{bmatrix} \bar{V}_{C_s}(t) \\ \bar{I}_{L_{ch}}(t) \\ \bar{V}_{C_{sh}}(t) \\ \bar{I}_{L_s}(t) \end{bmatrix}_{4N\times 1}, \tag{2.39}$$

where

$$\bar{V}_{C_s}(t) = \begin{bmatrix} V_{C_{s,1}}(t) & V_{C_{s,2}}(t) & V_{C_{s,3}}(t) & \cdots & V_{C_{s,N}}(t) \end{bmatrix}_{1\times N}^{T}, \tag{2.40}$$

$$\bar{I}_{L_{ch}}(t) = \begin{bmatrix} I_{L_{ch,1}}(t) & I_{L_{ch,2}}(t) & I_{L_{ch,3}}(t) & \cdots & I_{L_{ch,N}}(t) \end{bmatrix}_{1\times N}^{T}, \tag{2.41}$$

$$\bar{V}_{C_{sh}}(t) = \begin{bmatrix} V_{C_{sh,1}}(t) & V_{C_{sh,2}}(t) & V_{C_{sh,3}}(t) & \cdots & V_{C_{sh,N}}(t) \end{bmatrix}_{1\times N}^{T}, \tag{2.42}$$

$$\bar{I}_{L_s}(t) = \begin{bmatrix} I_{L_{s,1}}(t) & I_{L_{s,2}}(t) & I_{L_{s,3}}(t) & \cdots & I_{L_{s,N}}(t) \end{bmatrix}_{1\times N}^{T}. \tag{2.43}$$

By considering the coupling between the amplifiers, the following set of differential equations can be written for load inductors currents

$$\begin{cases} L_{s,1}\frac{dI_{L_{s,1}}}{dt} + M_{1,2}\frac{dI_{L_{s,2}}}{dt} + \cdots + M_{1,N}\frac{dI_{L_{s,N}}}{dt} = V_{C_{sh,1}} - V_{s,1} - R_{L,1}I_{L_{s,1}} \\ M_{2,1}\frac{dI_{L_{s,1}}}{dt} + L_{s,2}\frac{dI_{L_{s,2}}}{dt} + \cdots + M_{2,N}\frac{dI_{L_{s,N}}}{dt} = V_{C_{sh,2}} - V_{s,2} - R_{L,2}I_{L_{s,2}} \\ \vdots \\ M_{N,1}\frac{dI_{L_{s,1}}}{dt} + M_{N,2}\frac{dI_{L_{s,2}}}{dt} + \cdots + L_{s,N}\frac{dI_{L_{s,N}}}{dt} = V_{C_{sh,N}} - V_{s,N} - R_{L,N}I_{L_{s,N}}, \end{cases} \tag{2.44}$$

where $M_{m,n}$ represents the mutual inductance between m^{th} and n^{th} amplifiers. Equation. 2.44 can also be expressed as following

$$\bar{\bar{M}}\frac{d\bar{I}_{L_s}(t)}{dt} = \bar{V}_{C_{sh}}(t) - \bar{V}_{C_s}(t) - \bar{\bar{R}}_L\bar{I}_{L_s}(t), \tag{2.45}$$

$$\frac{d\bar{I}_{L_s}(t)}{dt} = \bar{\bar{M}}^{-1}\bar{V}_{C_{sh}}(t) - \bar{\bar{M}}^{-1}\bar{V}_{C_s}(t) - \bar{\bar{M}}^{-1}\bar{\bar{R}}_L\bar{I}_{L_s}(t), \tag{2.46}$$

where

$$\bar{\bar{M}} = \begin{bmatrix} L_{s,1} & M_{1,2} & \ldots & M_{1,N} \\ M_{2,1} & L_{s,2} & \ldots & M_{2,N} \\ \vdots & \vdots & \ddots & \vdots \\ M_{N,1} & M_{N,2} & \ldots & L_{s,N} \end{bmatrix}, \quad \bar{\bar{R}}_L = diag(R_{L,1}, R_{L,2}, \ldots, R_{L,N}), \tag{2.47}$$

and diag(a,b) provides a diagonal matrix with diagonal elements a and b.

Each period can be discretized into small time intervals, therefore, the state-space representation of the system in k^{th} time interval can be obtained by using the following differential equation:

$$\frac{d\bar{x}(t)}{dt} = \bar{\bar{A}}_k\bar{x}(t) + \bar{b} \qquad t_{k-1} \leq t \leq t_k, \tag{2.48}$$

where $\bar{\bar{A}}_k$ is the state matrix and it's elements depend on the switches' state and $\bar{b}$ is the input vector and it's elements are only function of circuit parameters over a period. The state matrix and the input vector can be written as:

$$\bar{\bar{A}}_k = \begin{bmatrix} \bar{\bar{0}} & \bar{\bar{0}} & \bar{\bar{0}} & \bar{\bar{\Sigma}}_1 \\ \bar{\bar{0}} & \bar{\bar{0}} & \bar{\bar{\Sigma}}_2 & \bar{\bar{0}} \\ \bar{\bar{0}} & \bar{\bar{\Sigma}}_3 & \bar{\bar{\Sigma}}_k & \bar{\bar{\Sigma}}_4 \\ -\bar{\bar{M}}^{-1} & \bar{\bar{0}} & \bar{\bar{M}}^{-1} & -\bar{\bar{M}}^{-1}\bar{\bar{R}}_L \end{bmatrix}_{4N\times 4N}, \quad \bar{b} = \begin{bmatrix} \bar{0} \\ \bar{b}_2 \\ \bar{0} \\ \bar{0} \end{bmatrix}_{1\times 4N}, \tag{2.49}$$

where $\bar{\bar{0}}$ and $\bar{0}$ indicate $N \times N$ and $1 \times N$ zero matrices, respectively. Here, the elements of $\bar{\bar{A}}_k$ and $\bar{b}$ are given as:

$$\bar{\bar{\Sigma}}_1 = diag(\frac{1}{C_{s,1}}, \frac{1}{C_{s,2}}, ..., \frac{1}{C_{s,N}}), \tag{2.50}$$

$$\bar{\bar{\Sigma}}_2 = diag(-\frac{1}{L_{ch,1}}, -\frac{1}{L_{ch,2}}, ..., \frac{1}{L_{ch,N}}), \tag{2.51}$$

$$\bar{\bar{\Sigma}}_3 = -\bar{\bar{\Sigma}}_4 = diag(\frac{1}{C_{sh,1}}, \frac{1}{C_{sh,2}}, ..., \frac{1}{C_{sh,N}}), \tag{2.52}$$

$$\bar{\bar{\Sigma}}_k = diag(-\frac{1}{R_{dson}C_{sh,1}}, -\frac{1}{R_{dson}C_{sh,2}}, ..., -\frac{1}{R_{dson}C_{sh,N}}) \times diag(\bar{U}_k), \tag{2.53}$$

$$\bar{b}_2 = \begin{bmatrix} \frac{V_{dc,1}}{L_{ch,1}} & \frac{V_{dc,2}}{L_{ch,2}} & \dots & \frac{V_{dc,N}}{L_{ch,N}} \end{bmatrix}^T_{1\times N}. \tag{2.54}$$

As mentioned before, $\bar{\bar{A}}_k$ is a time-varying matrix, dependent on the switching state. The only element of $\bar{\bar{A}}_k$ that varies by time is $\bar{\bar{\Sigma}}_k$ matrix, which is dependent on the switching vector, $\bar{U}_k$. It is noted that the elements of $\bar{U}_k$ are 0 or 1 according to the switches' status (off or on) in each time interval.

The solution of Eq. 2.48 can be expressed as:

$$\bar{x}(t) = \begin{cases} \bar{x}_1(t) \equiv e^{\bar{\bar{A}}_1 t}\bar{x}(0) + \bar{\bar{A}}_1^{-1}(e^{\bar{\bar{A}}_1 t} - I)\bar{b} & 0 \leq t \leq t_1, \\ \bar{x}_2(t) \equiv e^{\bar{\bar{A}}_2 (t-t_1)}\bar{x}(t_1) + \bar{\bar{A}}_2^{-1}(e^{\bar{\bar{A}}_2 (t-t_1)} - I)\bar{b} & t_1 \leq t \leq t_2, \\ \vdots & \\ \bar{x}_n(t) \equiv e^{\bar{\bar{A}}_n (t-t_{n-1})}\bar{x}(t_{n-1}) + \bar{\bar{A}}_n^{-1}(e^{\bar{\bar{A}}_n (t-t_{n-1})} - I)\bar{b} & t_{n-1} \leq t \leq t_n = T, \end{cases} \tag{2.55}$$

where n determines the number of time intervals and it is enough to plot the waveforms with a similar resolution to the circuit simulators. By considering the steady-state condition, $\bar{x}(0) = \bar{x}_1(0) = \bar{x}_n(t_n = T)$, and defining $\bar{\bar{F}}_k(t)$ and $\bar{q}_k(t)$ as

$$\bar{\bar{F}}_k(t) = e^{\bar{\bar{A}}_k(t-t_{k-1})}, \quad \bar{q}_k(t) = \bar{\bar{A}}_k^{-1}(e^{\bar{\bar{A}}_k(t-t_{k-1})} - I)\bar{b}, \quad 0 \leq t_k \leq T, \tag{2.56}$$

the initial value of $\bar{x}$ is calculated as

$$\begin{aligned} \bar{x}(0) = &\Big(I - \bar{\bar{F}}_n(t_n)\bar{\bar{F}}_{n-1}(t_{n-1}) \ldots \bar{\bar{F}}_1(t_1)\Big)^{-1} \\ &\times \Big(\bar{\bar{F}}_n(t_n)\bar{\bar{F}}_{n-1}(t_{n-1}) \ldots \bar{\bar{F}}_2(t_2)\bar{q}_1(t_1) + \bar{\bar{F}}_n(t_n)\bar{\bar{F}}_{n-1}(t_{n-1}) \ldots \\ &\bar{\bar{F}}_3(t_3)\bar{q}_2(t_2) + \cdots + \bar{\bar{F}}_n(t_n)\bar{q}_{n-1}(t_{n-1}) + \bar{q}_n(t_n)\Big). \end{aligned} \tag{2.57}$$

Therefore, by using the above results, the dynamics of the system in the steady-state can be simulated in MATLAB. In addition, the input and output power, and the efficiency of the whole system can be found by the following formulas [10]:

$$\begin{aligned} \text{Total output RF power} = \sum_{i=1}^{N} P_{R_{L,i}} &= \frac{R_{L,1}}{T}\int_0^T I^2_{L_{s,1}}(t)\,dt \\ &+ \frac{R_{L,2}}{T}\int_0^T I^2_{L_{s,2}}(t)\,dt + \cdots + \frac{R_{L,N}}{T}\int_0^T I^2_{L_{s,N}}(t)\,dt, \end{aligned} \tag{2.58}$$

$$\begin{aligned} \text{Total input DC supply power} = \sum_{i=1}^{N} P_{V_{dc,i}} &= \frac{V_{dc,1}}{T}\int_0^T I_{L_{ch,1}}(t)\,dt \\ &+ \frac{V_{dc,2}}{T}\int_0^T I_{L_{ch,2}}(t)\,dt + \cdots + \frac{V_{dc,N}}{T}\int_0^T I_{L_{ch,N}}(t)\,dt, \end{aligned} \tag{2.59}$$

$$\text{Total efficiency} = \eta_{total} = \frac{\text{Total Output RF power}}{\text{Total input DC supply power}} = \frac{P_{R_L}}{P_{V_{dc}}}. \tag{2.60}$$

2.4 Transient Behavior Analysis of Array of Class-E Amplifiers with Coupled Loads

In this section, the state-space model is used to investigate the system's behavior before reaching its steady-state. Since the input signals of the amplifiers (gate and supply signals) may be changed suddenly, therefore, the time takes to reach steady-state is important. By using Eq. 2.55 and Eq. 2.56, the system from the beginning of the period to the end of a period can be described using the following set of equations:

$$\begin{cases} \bar{x}_1 = \bar{\bar{F}}_1 \bar{x}_0 + \bar{q}_1, \\ \bar{x}_2 = \bar{\bar{F}}_2 \bar{x}_1 + \bar{q}_2. \\ \vdots \\ \bar{x}_{n-1} = \bar{\bar{F}}_{n-1} \bar{x}_{n-2} + \bar{q}_{n-1}, \\ \bar{x}_n = \bar{\bar{F}}_n \bar{x}_{n-1} + \bar{q}_n, \end{cases} \tag{2.61}$$

As mentioned above, Eq. 2.61 provides a set of difference equations which represent the dynamics of the system from the beginning to the end of each period. In order to indicate the period number, we add another subscript, e.g. $\bar{x}_{0,p}$, $\bar{x}_{1,p}$, ..., $\bar{x}_{n,p}$ for the p^{th} period instead of $\bar{x}_0$, $\bar{x}_1$, ..., $\bar{x}_n$ in Eq. 2.61.

Investigating the behavior of the dynamics at the end of each period equips us with some tools to analyze the transient behavior of the system. To this end, we define $\bar{X}_p$ as the value of $\bar{x}$ at the end of p^{th} period, that is, $\bar{X}_p \equiv \bar{x}_{n,p}$. Therefore, the dynamics of the sampled-data at the end of each period can be given as

$$\bar{X}_{p+1} = \bar{\bar{C}} \bar{X}_p + \bar{d}, \tag{2.62}$$

with the initial condition $\bar{X}_0 \equiv \bar{x}_{0,1}$, where

$$\bar{\bar{C}} = \bar{\bar{F}}_{p,n} \bar{\bar{F}}_{p,n-1} \bar{\bar{F}}_{p,n-2} \dots \bar{\bar{F}}_{p,1}, \tag{2.63}$$

$$\bar{d} = \bar{\bar{F}}_{p,n} \bar{\bar{F}}_{p,n-1} \dots \bar{\bar{F}}_{p,1} \bar{q}_{p,2} + \dots + \bar{\bar{F}}_{p,n} \bar{\bar{F}}_{p,n-1} \bar{q}_{p,n-2} + \bar{\bar{F}}_{p,n} \bar{q}_{p,n-1} + \bar{q}_{p,n}. \tag{2.64}$$

To clarify this sampling process, a continuous process (blue line) and its sampled-data at each T sampling time is illustrated in Fig. 2.5.

Equation 2.62 is a key equation for analyzing the transient response of the system, since it provides important information about the system like time constant,

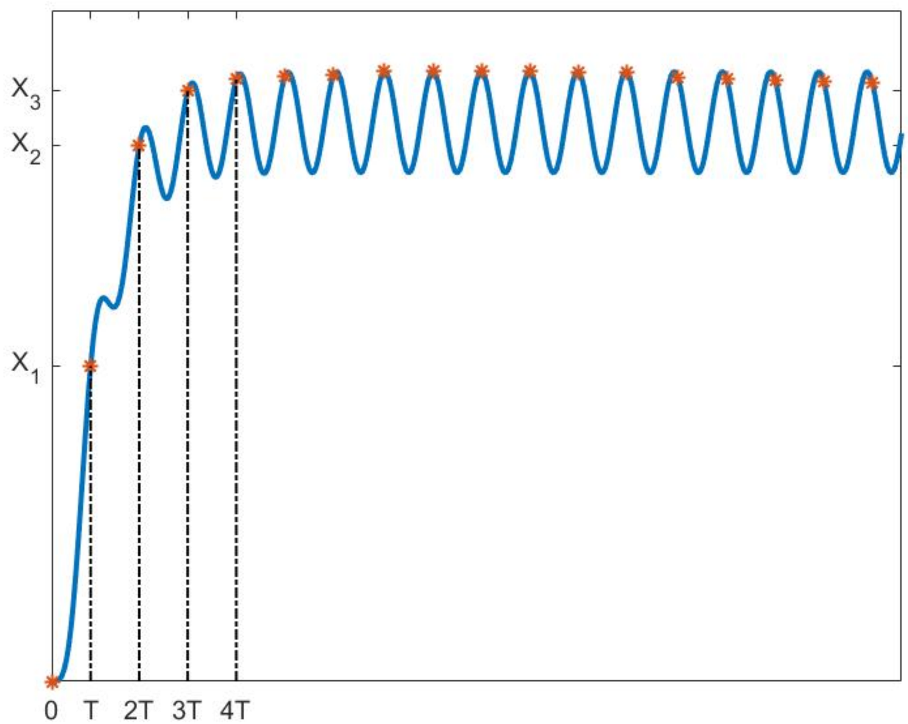

Figure 2.5: A simulation example demonstrating the continuous and the sampled-data dynamics, suppose that X is the state of the system and X_1, X_2, and X_3 are its values at sampling times, T, $2T$, and $3T$, respectively

settling time. Using this information, one can measure how fast the dynamics reach its steady state.

The first step for analyzing the dynamics of Eq. 2.62 is to check whether it remains stable. This can be achieved by finding the eigenvalues of $\bar{\bar{C}}$. Once the eigenvalues of $\bar{\bar{C}}$ are inside the unit circle, we can guarantee that the dynamic is asymptotically stable and $\bar{X}_p$ reaches its steady-state as p increases.

Consider λ_i as the i^{th} eigenvalue of $\bar{\bar{C}}$, and define $a = \max_i |Re\{\lambda_i\}|$. Assuming that $0 \leq a < 1$, the time constant of the system 2.62 can be calculated by comparing the response of discrete and continuous systems as [34]

$$e^{-t/\tau} = a^n \quad \rightarrow \quad e^{-t/\tau} = (e^{ln(a)})^n = e^{n\,ln(a)} \quad \rightarrow \quad \frac{-t}{\tau} = n\,ln(a). \tag{2.65}$$

Since we are sampling at the end of each period, we substitute $t = nT$, thus we get the maximum time constant of the system, τ, as

$$\frac{-nT}{\tau} = n\,ln(a) \quad \rightarrow \quad \tau = \frac{-T}{ln(a)}. \tag{2.66}$$

Notice that the response of a stable system reaches 98% of its steady-state at about 4τ [35]. Using this approach, one can find the time constant by observing the response of the system.

By changing the coordinate of the state space model, we can look at the dynamics of the system from a new point of view. Suppose that $Z_p = \bar{\bar{T}}X_p$, where $\bar{\bar{T}}$ is a non-singular matrix. Then, we have

$$Z_{p+1} = \bar{\bar{T}}X_{p+1} = \bar{\bar{T}}\bar{\bar{C}}\bar{X}_p + \bar{\bar{T}}\bar{d} = \bar{\bar{T}}\bar{\bar{C}}\bar{\bar{T}}^{-1}\bar{Z}_p + \bar{\bar{T}}\bar{d}. \tag{2.67}$$

This change of coordinate also retains the eigenvalues of the system,

$$\begin{aligned} |\lambda I - \bar{\bar{T}}\bar{\bar{C}}\bar{\bar{T}}^{-1}| &= |\lambda\bar{\bar{T}}\bar{\bar{T}}^{-1} - \bar{\bar{T}}\bar{\bar{C}}\bar{\bar{T}}^{-1}| = |\bar{\bar{T}}(\lambda I - \bar{\bar{C}})\bar{\bar{T}}^{-1}| \\ &= |\bar{\bar{T}}||\lambda I - \bar{\bar{C}}||\bar{\bar{T}}^{-1}| = |\lambda I - \bar{\bar{C}}|, \end{aligned} \tag{2.68}$$

where $|\cdot|$ calculates the determinant of a matrix.

Consider that $\bar{\bar{C}}$ has distinct eigenvalues. By defining $\bar{\bar{T}}$ as

$$\bar{\bar{T}} = [\bar{v}_1, ..., \bar{v}_n], \tag{2.69}$$

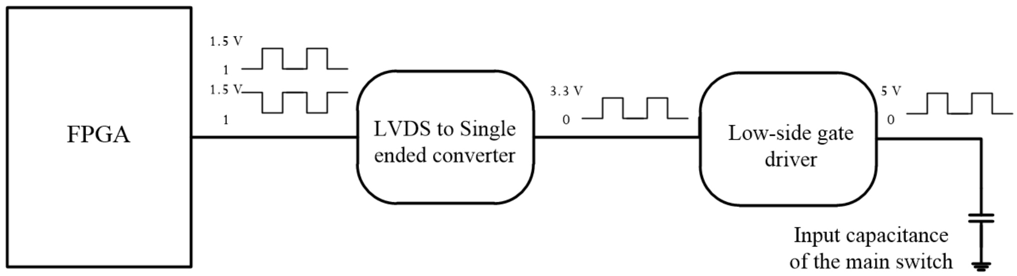

Figure 2.6: The proposed driver diagram

where $\bar{v}_1$, ..., $\bar{v}_n$ are the independent eigenvectors of $\bar{\bar{C}}$, the change of coordinate leads to the diagonalization of the system [36]

$$\bar{\bar{T}}\bar{\bar{C}}\bar{\bar{T}}^{-1} = \begin{bmatrix} \lambda_1 & & 0 \\ & \ddots & \\ 0 & & \lambda_n \end{bmatrix}. \tag{2.70}$$

2.4.1 Driver

The class-E power amplifier can be controlled digitally [28]. FPGA (XILINX Inc., KCU105, California, USA) is used to generate and send digital signals to the amplifier using low voltage differential signaling (LVDS) since it can improve the noise performance. The input signal's frequency is 64MHz, and phase delay can be added to the signal by FPGA. A two-stage driver circuit is designed to receive FPGA outputs and supply the proper voltage and current levels to turn on and off the switch. The block diagram of the designed driver is illustrated in Fig. 2.6.

The driver receives a pair of LVDS signals and then converts them into a 0-3.3V single-ended signal as an input to a low-side gate driver [31], which provides enough levels of the voltage and current to charge and discharge the switch's input capacitance. Using only a pair of LVDS signals, a low-side gate driver can improve the input signal's voltage level up to its supply 0-5V and provide enough output current.

2.4.2 Supply Modulation

As explained in the previous section, FPGA controls the phase and frequency of the input signals into the driver circuit. To enhance the amplifier's efficiency, envelope modulation must be applied to the pulse [37]. It can have a particular shape, such as Sinc, Gaussian, or triangular. It can be written in the following form

$$f(t) = A(t)sin(2\pi f_o t + \phi), \tag{2.71}$$

where $A(t)$, f_o, and ϕ are desired envelope modulation, carrier frequency, and phase of modulated pulse, respectively.

The supply modulation method is used for envelope modulation purposes. Using this method, the load voltage is linearly proportional to the supply voltage in the ideal case, but in reality, it is not linear due to the switch. To address this issue, a feedback circuitry such as a buck converter as proposed in [21] can be utilized. This work uses a half-bridge converter instead of a buck converter, as explained in [28]. It consists of two switches and a filter. For designing the half-bridge, it should be noted that the switching frequency must be larger than the bandwidth of the envelope. In addition, the low pass filter's delay should be kept at its minimum while it can adequately filter the switching frequency component. Therefore, the switching frequency of 1MHz is considered. In a half-bridge

$$V_o = V_{dc}\, D, \tag{2.72}$$

where D is the duty cycle, it can be calculated in MATLAB to acquire different pulse shapes. Considering a 5nsec step size in FPGA, the output of the half-bridge circuit changes between 5% to 95% of V_{dc} with $0.005V_{dc}$ resolution. The bitstream is generated in MATLAB and then sent to FPGA, which controls the PWM of the half-bridge circuit [28, 29].

The block diagram of supply modulatıon is illustrated in Fig. 2.7. Firstly, the circuit receives a pair of LVDS signals from FPGA and then converts them to a single-ended signal 0-3.3V. In the second stage, the single-ended signal is given to a switch driver, which provides high and low side signals to turn on and off

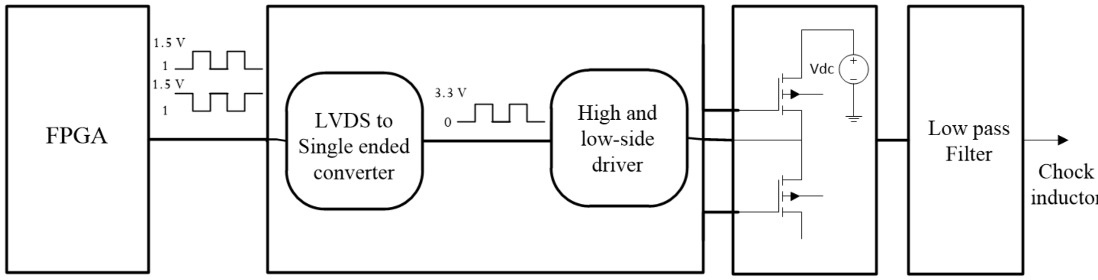

Figure 2.7: Supply modulation diagram

the switches. A low pass filter is implemented in the last stage to smooth out the output.

Chapter 3

Methods

This chapter presents methods for analyzing the operation of class-E amplifiers using the state-space model. The details of simulations in MATLAB and LT-SPICE are given. Transient analysis of the system using the state-space model is also explained. Next, the class-E amplifier's hardware design, simulations, and implementation are presented in detail. Finally, the experimental setup for testing the PCB and measuring power and efficiency is described.

3.1 State-Space Model Simulations

The state-space model of an array of class-E amplifiers with coupled coils is developed in MATLAB. This model provides current and voltage waveforms of state variables, input and output powers, and efficiency of each amplifier and the whole array. The reliability of the state-space model is validated by comparing its results with LTSPICE simulation results. For a single class-E amplifier, the effect of series and shunt capacitors' variations on the efficiency and power is shown. The time constant of the amplifier (considering choke inductor current) is calculated using state-space model, and the result is compared with LTSPICE. The frequency response of the amplifier is also found using the state-space model and LTSPICE data.

A two class-E amplifiers with coupled coils are also simulated using the state-space model and the results are verified by simulating the same circuit in LT-SPICE and comparing the results. The efficiency and power of the system is also investigated regarding to phase delay and series capacitor values variations. The frequency response and time constant of the system are presented. Finally, the effect of input phase delays on output power, efficiency and time constant of a three channel class-E amplifiers with coupled coils is provided.

3.2 Hardware Implementation

The hardware implementation process contains competent selection, simulations, and layout design. The main switch is selected based on some key factors that are given as follows. It should have a low on-resistance compared to the load to decrease switch losses. Since the amplifier operates at 64MHz, charging and discharging large capacitance values with low rise and fall times are difficult. Therefore, the switch input capacitance should be as small as possible. Additionally, the maximum drain to source voltage ($V_{ds_{max}}$) should be high enough because the drain voltage of the Class-E amplifier can increase up to $3.56V_{dc}$ [28]. Considering these factors, the Gallium Nitride (GaN) power FET, EPC2036, is selected as the main switch for this design. It has low on-resistance (R_{dson} =73mΩ), and its maximum drain to source voltage is 100V. The other advantages of EPC2036 are its small size (0.9mm$\times$0.9mm) that shrinks the PCB size, and its low price, which leads to a cost-efficient final product. The design blocks are illustrated in Fig. 3.1.

3.2.1 Driver Implementation

The driver circuit is designed in 2-stages and is implemented with an LVDS to single-ended converter, a low-side gate driver, as illustrated in Fig. 3.2.

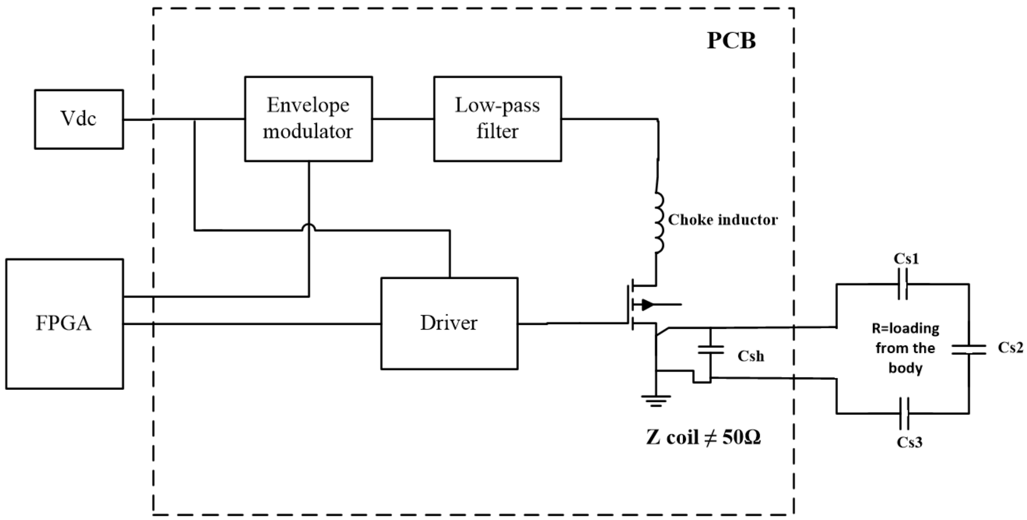

Figure 3.1: Amplifier's block and the components

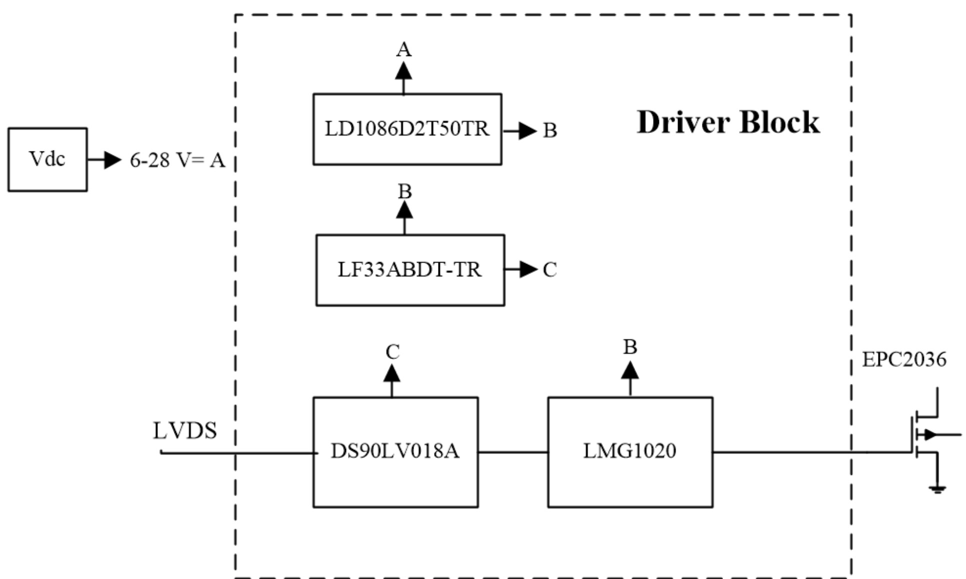

Figure 3.2: Driver block and the components

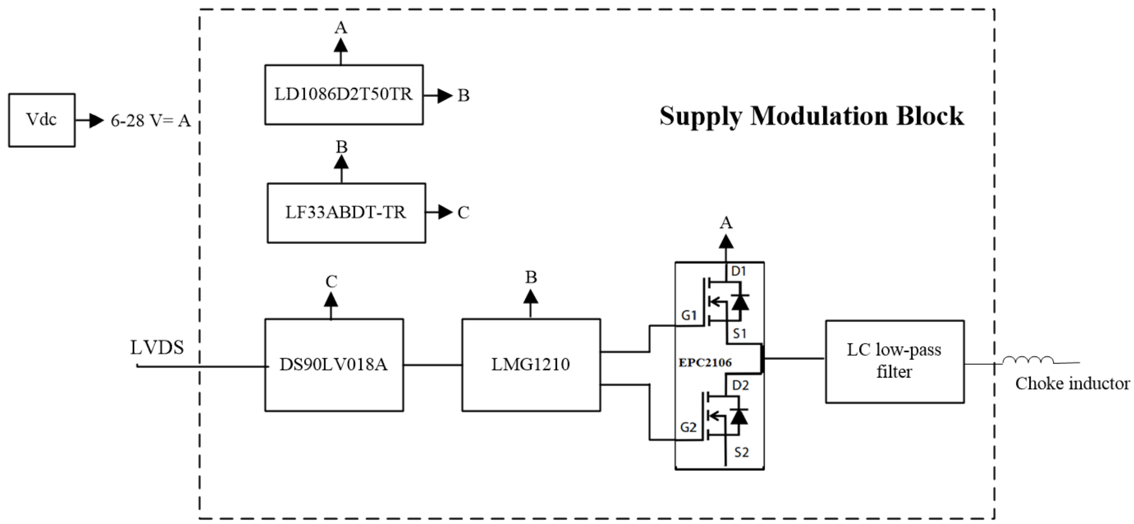

Figure 3.3: Supply modulation block and the components

DS90LV018A is a low-power, low-noise LVDS to a single-ended converter that supports high switching rates. In the first stage, it receives 64 MHz LVDS signals and then provides a 0-3.3V single-ended signal as the input to the LMG1020 device. LMG1020 is a single, low-side driver which can derive Gallium Nitride Field Effect Transistor (GaN FET) in high frequencies. The supply voltage of this integrated circuit (IC) is 5V, and it can supply the output signal 0-5V with enough current level to charge and discharge the input capacitance of the switch (75pF). The rise and fall time of the output signal is less than 1ns.

3.2.2 Supply Modulation Implementation

The supply modulation block and its components are shown in Fig. 3.3. It consists of an LVDS to single-ended converter, a half-bridge gate driver, two switches, and an LC low-pass filter.

DS90LV018A receives LVDS signals and converts into a single ended signal 0-3.3V. Then the signal is given into LMG1210 which is half-bridge MOSFET and Gallium Nitride Field Effect Transistor (GaN FET). It has two control input modes, Independent Input Mode (IIM) and PWM mode. In IIM, the outputs can be controlled independently using two input signals while in PWM mode, the output signals can be generated using a single input signal. In our case, since there is only one input signal into LMG1210, PWM mode is used. In PWM mode, the dead time can be adjusted from 0 to 20ns for each edge. For the half bridge, EPC2106 is used which is an enhancement-mode monolithic GaN transistor and it includes two low on-resistance eGaN power FETs. Using this low cost IC, prevents the interconnect inductances and the interstitial space needed on the PCB.

Finally, an LC low pass filter which is built from 1uF capacitor and 2uH air core inductor is made to decrease ripple of the modulated signal. Two parallel 2Ω damping resistors are used in the filter to increase stability of the system and prevent switching overvoltage [38].

3.2.3 Hardware Simulations

In order to make sure that the amplifier works properly, the designed circuit is simulated in LTSPICE (see Fig. 3.4) and Advanced Design System 2021 (ADS) (see Fig. 3.5). In the LTSPICE simulation, DS90LV018A model can not be imported, therefore, instead of using this IC, a pulse signal generator (64MHz, 0-3.3V) is placed to simulate the output of this stage.

3.2.4 Layout Implementation

The PCB layout of designed circuit is drawn in Proteus 8.0 software. The schematic and and layout of the circuit are illustrated in Fig 3.6 and Fig 3.7 respectively. As explained in the previous sections, the whole amplifier design consists of driver, main switch, supply modulations, power regulators, and the filter. In order to make an efficient board while working properly, several factors are considered during designing the PCB such as minimizing the space between

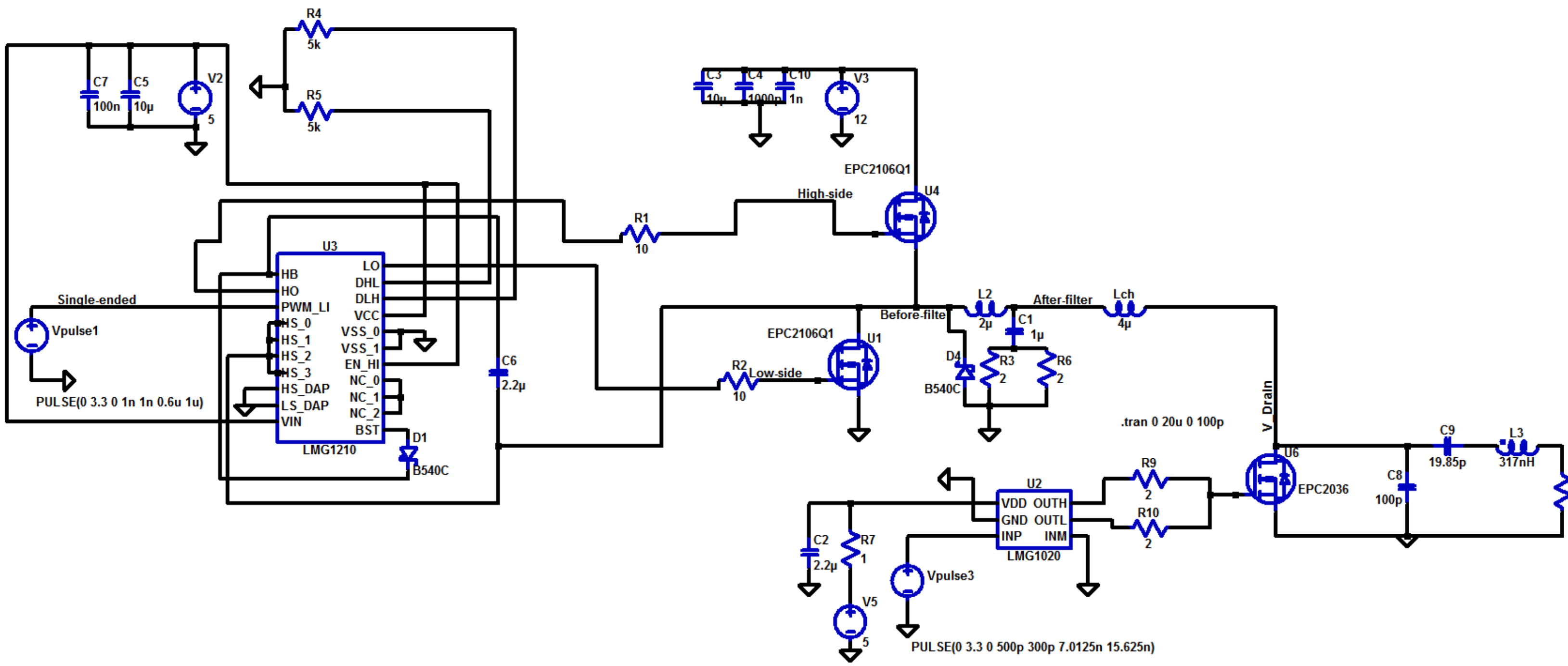

Figure 3.4: Schematic of the amplifier in LTSPICE

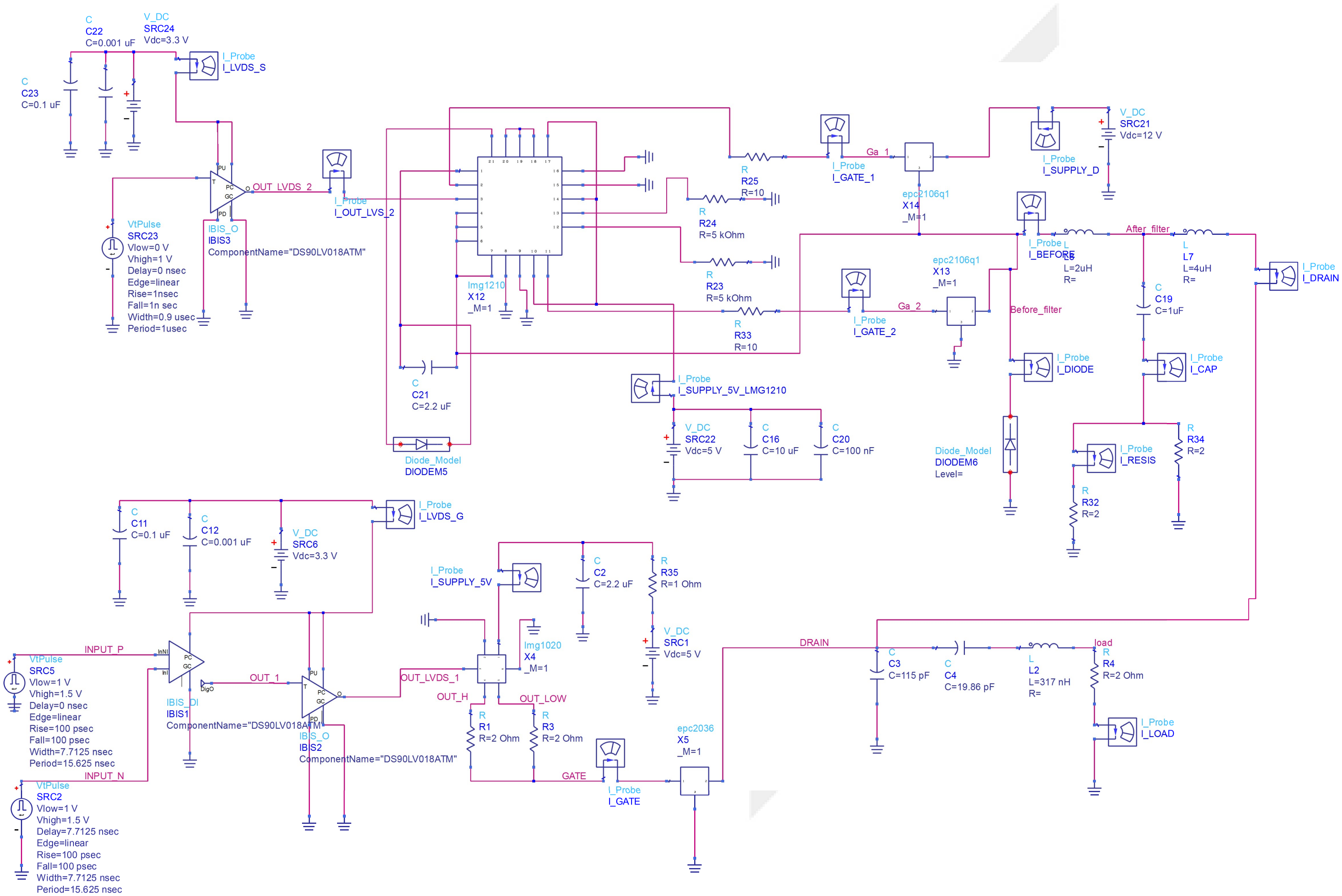

Figure 3.5: Schematic of the amplifier in ADS

components as possible while there is no interference on their operation, proper grounding, and including some test points on the board. In addition, some sensitive ICs are used in this design, therefore, it is very important to consider the manufacture's recommendations in data sheet for the layout design.

Finally, by considering our circuit's features, a four-layer PCB is designed. The top layer contains components and signal traces, the second and fourth layer are the ground, and the third layer includes DC signal traces. The board thickness and dimensions are 1.48mm and 66.02mm x 32.74mm respectively. 3D illustration of the circuit is shown in Fig. 3.8.

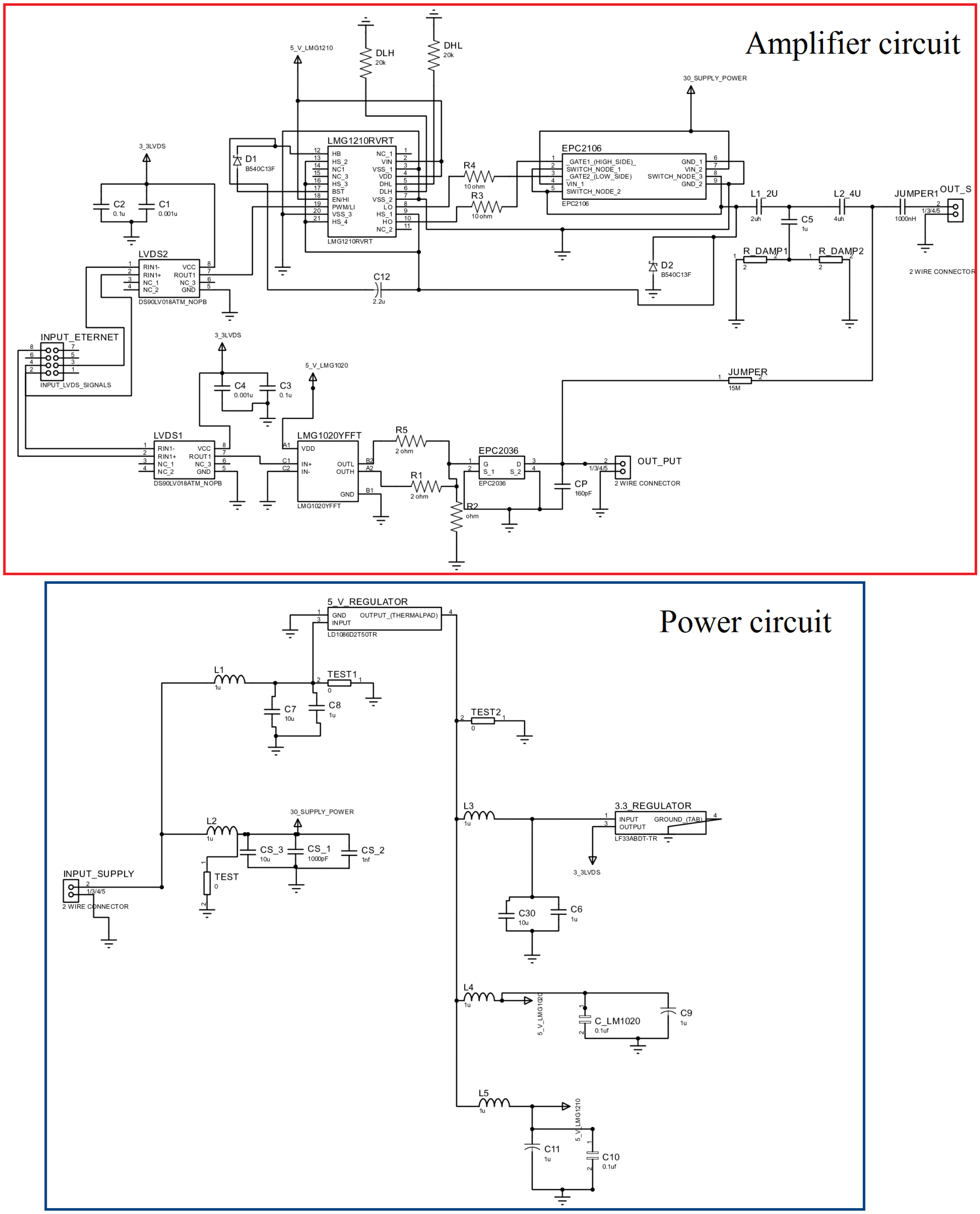

Figure 3.6: Schematic of the circuit in Proteus

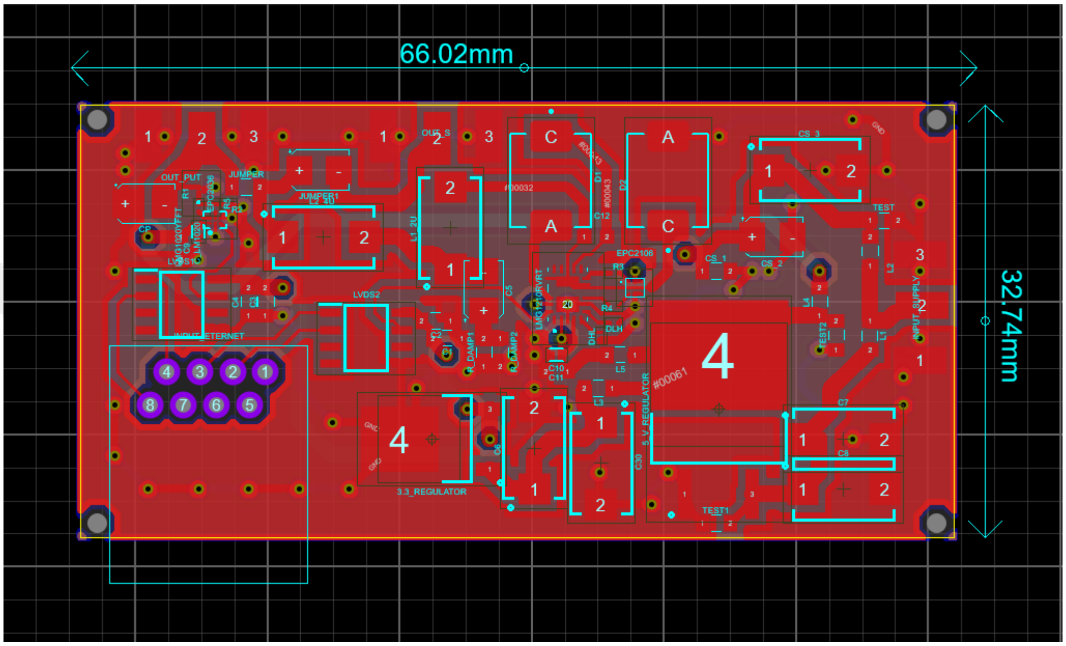

Figure 3.7: Layout of the circuit

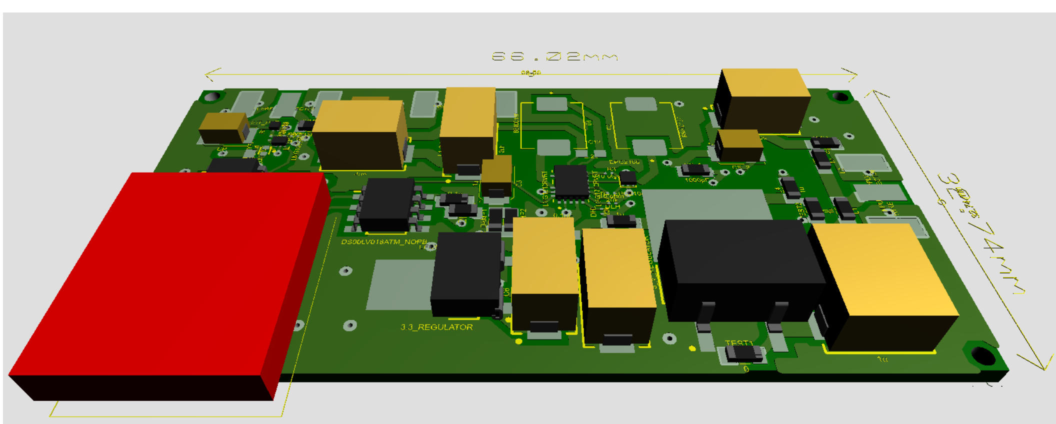

Figure 3.8: 3D illustration of the designed PCB

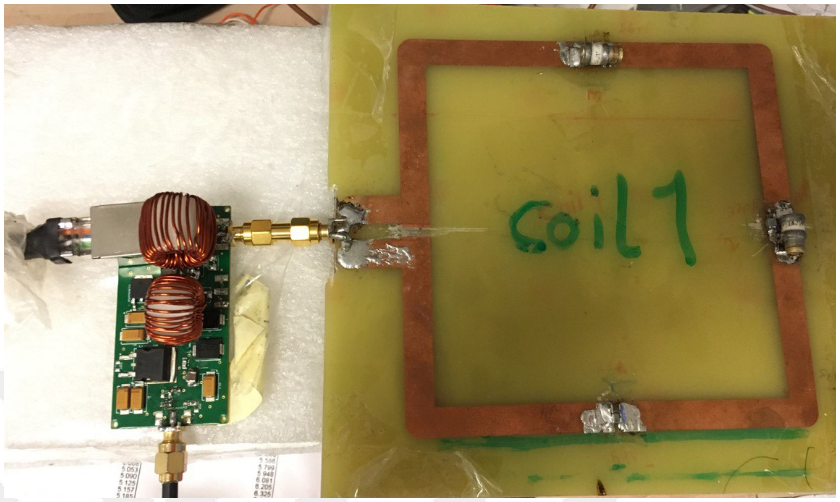

Figure 3.9: Class-E amplifier's PCB with a transmit coil

3.3 Experimental Setup for Power and Efficiency Measurement

In this section, power and efficiency is measured for a single channel Class-E amplifier. The amplifier's PCB is connected to a rectangular loop-shape RF coil which is placed on top of a phantom as it is shown in Fig. 3.9.

The output power is found by measuring the power in a small pick up coil as can be seen from Fig. 3.10. The pick up coil is matched to 50Ω at 64MHz and it is placed close to the main coil. In order to find the relation between the pick up coil's power and the output power, S_{11} and S_{21} parameters are recorded using a network analyzer. It should also pointed out while recording the S-parameters, the main and pick up coils are connected to port 1 and port 2 of the network analyzer. Therefore, the output power can be found using the following equation

$$P_{out} = \alpha P_{pick-up}, \tag{3.1}$$

where $P_{pick-up}$ and α can be defined as

$$P_{pick-up} = \frac{V^2_{rms,pick-up}}{R_{pick_{u}p}}, \tag{3.2}$$

$$\alpha = \frac{1 - 10^{S_{11}}}{10^{S_{21}}}. \tag{3.3}$$

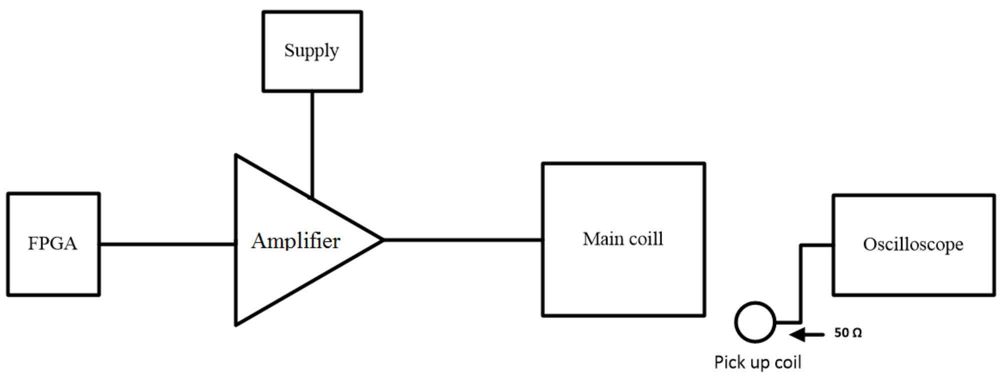

Figure 3.10: Power and efficiency measurement setup

Chapter 4

Results

In this chapter, simulation and experimental results are presented and compared with the state-space model. Firstly, the state-space model is employed to tune the capacitors of a single class-E amplifier. To verify the state-space model results, the circuit is simulated in LTSPICE. A comparison between these two results is also provided. Effects of shunt and series capacitors' values on the amplifier characteristics, such as output power and efficiency, are investigated. Secondly, the state-space model of two class-E amplifiers with significantly coupled coils is simulated, and the results are verified in LTSPICE. Also, using the state-space model, high efficiency and power modes of operation are found with respect to series capacitor values and phase delays between the gate signals of the amplifiers. Then, high efficiency and high power modes of operation for three class-E amplifiers with significantly coupled coils are investigated. Analysis of transient behavior of two and three class-E amplifiers is also given. Finally, the simulation and experimental results of the designed hardware for the amplifier are illustrated.

4.1 Single Class-E Amplifier

4.1.1 State-Space Model

The state-space model of a class-E amplifier is simulated in MATLAB. Some circuit parameters such as C_{sh} and C_s values are calculated theoretically [27] considering the transistor's model and coil measurement (R_L and L_s). The circuit parameters are as R_L=2Ω, L_s=317nH ,L_{ch}=5uH, V_{dc}=25V, C_{sh}=130pF, C_s=19.86pF, period (T)=15.625nsec, and duty cycle=50%.

It should be noted that the effect of the transistor's capacitor, which is parallel to C_{sh}, is considered in the state-space model. Therefore, the overall shunt capacitor value is calculated as 215pF instead of 130pF in MATLAB. The simulation is performed for two periods, and the differential equations are solved numerically by considering 2000 points per period. After providing circuit parameters to the state-space model, the steady-state waveforms of a single class-E amplifier are plotted as shown in Fig. 4.1. The input and output powers and efficiency of the amplifier are found as 183W, 174W, and 95%, respectively.

4.1.2 LTSPICE

To verify the simulation results of the state-space model, a circuit with the same parameters is simulated in LTSPICE as shown in Fig. 4.2. Figure 4.3 illustrates the waveforms of inductors' currents and capacitors' voltages in LTSPICE. The input and output power and efficiency are also computed for this circuit. Simulation results for the state-space model are compared with LTSPICE results in Tab. 4.1. It can be seen that the error between these two simulations is not significant. One reason for this error is that the estimated values of transistor's capacitor and on-resistor are used in MATLAB simulations. In addition, MATLAB generates an ideal pulse as a gate signal while in the LTSPICE, the gate signal is not an ideal pulse and its rise and fall times are 100psec, which may also affect the simulation results.

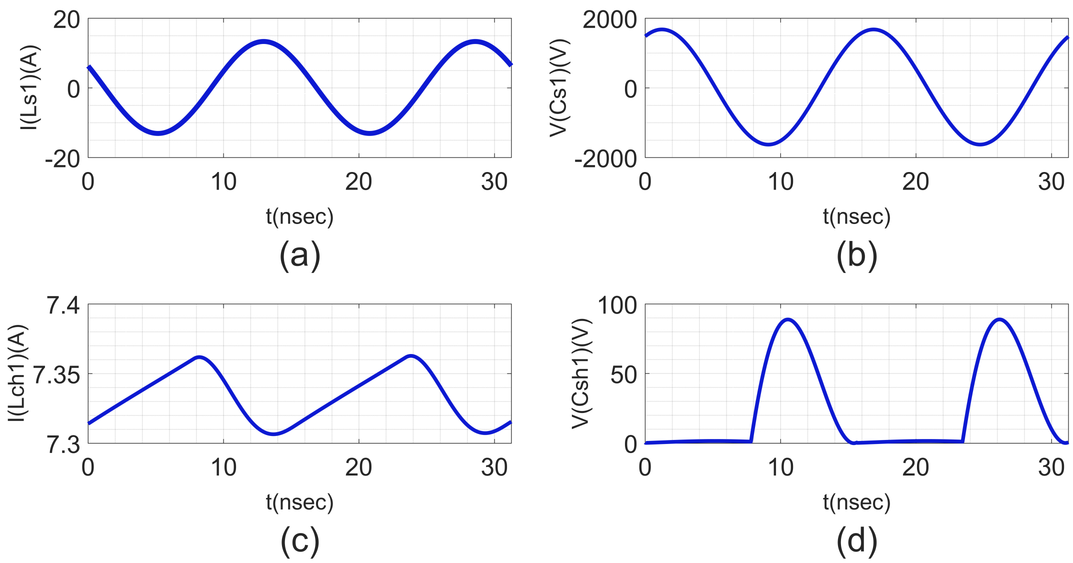

Figure 4.1: Steady-state waveforms of the class-E amplifier in MATLAB. (a) Series inductor current. (b) Series capacitor voltage. (c) Choke inductor current. (d) Shunt capacitor voltage.

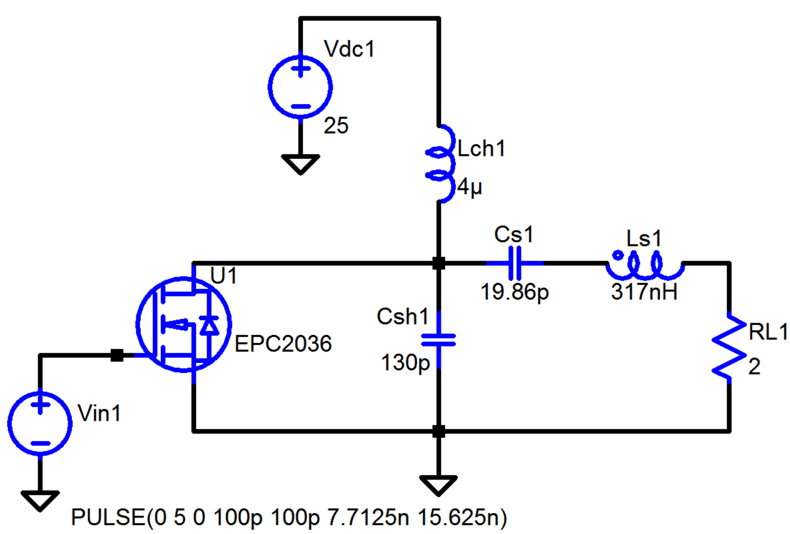

Figure 4.2: Schematic of the class-E amplifier in LTSPICE

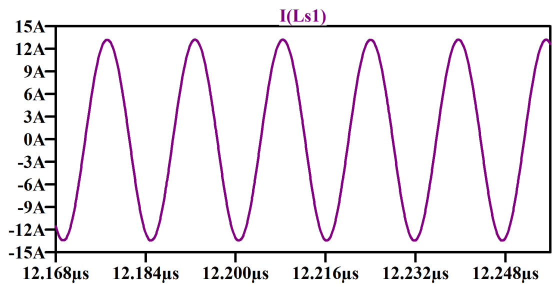

(a)

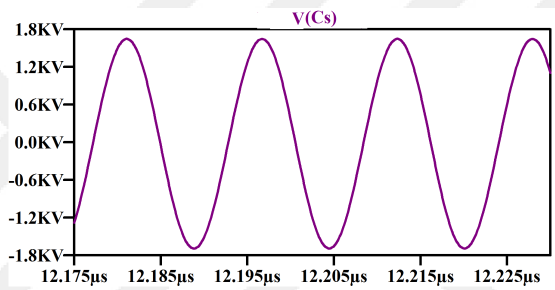

(b)

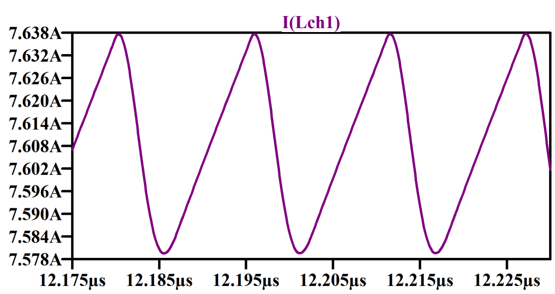

(c)

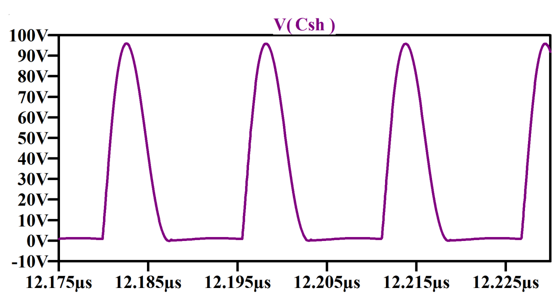

(d)

Figure 4.3: Waveforms of class-E amplifier in LTSPICE. (a) Series inductor current. (b) Series capacitor voltage. (c) Choke inductor current. (d) Shunt capacitor voltage.

Parameters	State-space Model	LTSPICE
$I_{L_{ch,1}}$ (average value)	7.3A	7.6A
$V_{C_{sh,1}}$ (peak value)	89V	96V
$V_{C_{s,1}}$ (peak value)	1673V	1691V
$I_{L_{s,1}}$ (peak value)	13.3A	13.2A
Input power	183W	190W
Output power	174W	177W
Efficiency	95%	93%

Table 4.1: Comparison of simulation results of the state-space model and LTSPICE (single class-E amplifier)

4.1.3 Tuning Series and Shunt Capacitors

A class-E amplifier can reach high efficiency when two conditions of zero-voltage switching (ZVS) and zero-voltage derivative switching (ZVDS) are satisfied as explained in Sec.2.1. In order to satisfy these conditions and achieve high efficiency, the series and shunt capacitors (C_s and C_{sh}) should be tuned. For the given single class-E amplifier, high efficiency operation points are investigated by swiping C_s and C_{sh} capacitors' values. The simulation is performed in MATLAB using the state-space model and the capacitors' values, C_{sh} and C_s, are swept from 80pF to 300pF and from 19.5pF to 20pF, respectively, as shown in Fig. 4.4. The swept range of C_s is considered smaller than the swept range of C_{sh}, since the amplifier's efficiency is more sensitive to the variation of C_s values.

It is observed in Fig. 4.4 that the efficiency is high enough for the most part of C_s and C_{sh} values ranges. However, there are some limitations such as the maximum drain voltage and drain current of the switching transistor (EPC2036), and the maximum power of the amplifier. Using EPC2036 datasheet, the maximum drain voltage and current are 110V and 18A in the pulsed mode. Also, the maximum power and efficiency of the amplifier are calculated as 225W and 96%, respectively. However, the power level that can be achieved is lower than 225W in practical due to transistor's current limit. Therefore, in addition to efficiency, it is important to consider the output power at the same time. The output power with respect to C_{sh} and C_s values is demonstrated in Fig. 4.5. Therefore, considering these figures and the limitations, the values of the capacitors can be found

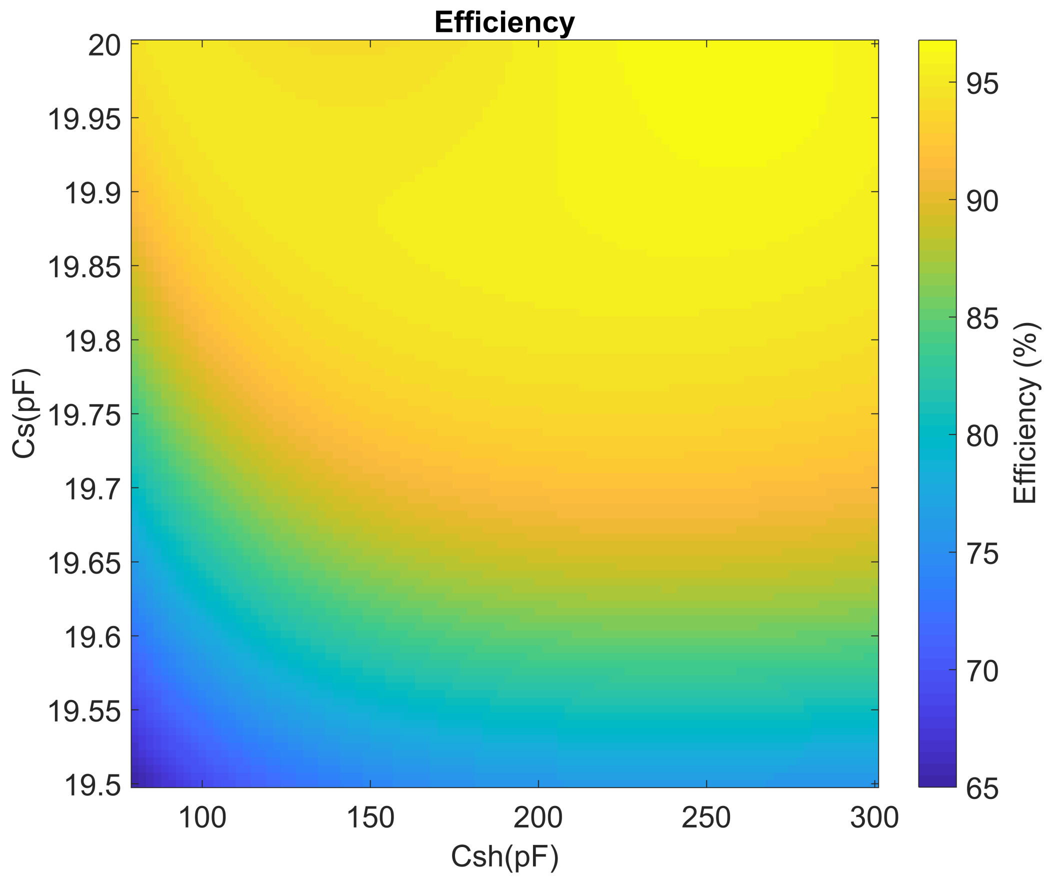

Figure 4.4: Efficiency of the class-E amplifier regarding shunt (C_{sh}) and series (C_s) capacitors' values

for high efficiency operation of the class-E amplifier.

4.1.4 Transient Analysis and Frequency Response

Figure 4.6 shows the choke inductor current ($I_{L_{ch}}$) for the class-E amplifier, used in Sec. 4.1.2. Consider the steady-state value of this current, which is 7.63A. In order to find the time constant, one can calculate 98% of the steady-state value ($0.98 \times 7.63 = 7.48$), and find its associated time (5.74μsec). These values are indicated in Fig. 4.6. Then, the time constant is calculated as $5.74/4 = 1.43\mu sec$. This result is consistent with the time constant, that is found by employing the state-space model (Eq. 2.66). The time constant using the state-space model is

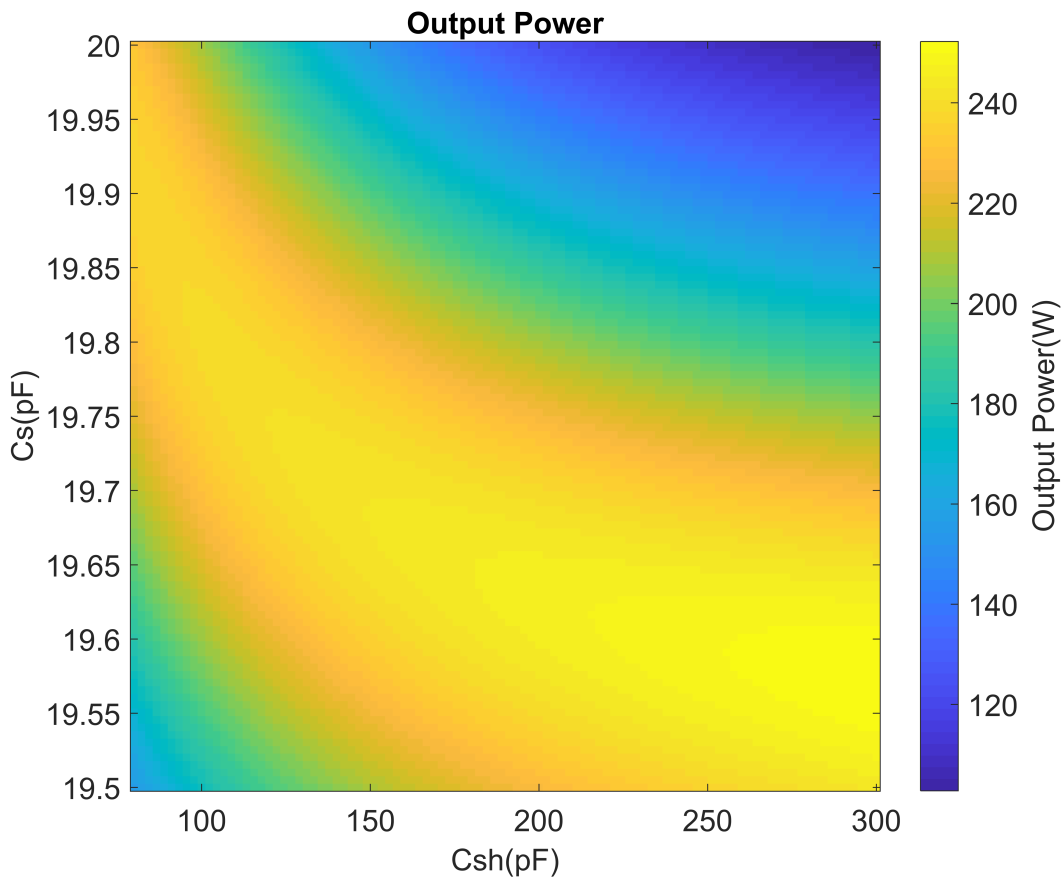

Figure 4.5: Output power of the class-E amplifier regarding shunt (C_{sh}) and series (C_s) capacitors' values

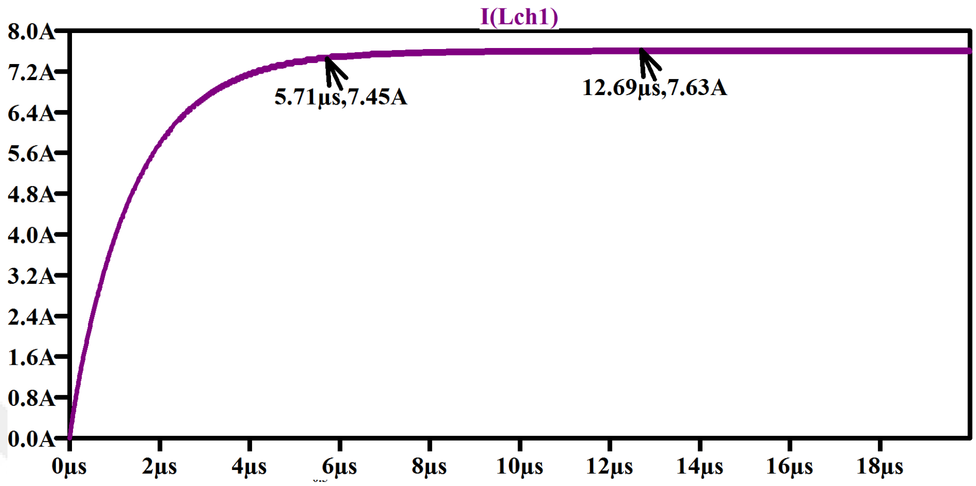

Figure 4.6: Choke inductor current versus time

calculated as 1.34μsec.

Figure 4.7 shows the amplifier's output power and efficiency with respect to frequency changes using the state-space model and LTSPICE data. It is seen that the proposed state-space model behaves similar to the LTSPICE data in terms of output power and efficiency.

4.2 Two Class-E Amplifiers with Significantly Coupled Coils

In this section, simulation results of two class-E amplifiers with significantly coupled coils are compared in the state-space model and LTSPICE. The simulations are performed considering two different scenarios. In the first scenario, high output power and efficiency are achieved for the amplifiers by adjusting series capacitors' values (C_{s1} and C_{s2}) while other circuits' parameters are the same. In the second scenario, high output power and efficiency are achieved for the similar amplifiers by introducing a phase delay between gates' signals. The coupling coefficient's value (k) is assumed as -0.1 in all simulations. Finally, the effects of series capacitor (C_s) values and phase delays are investigated on the output

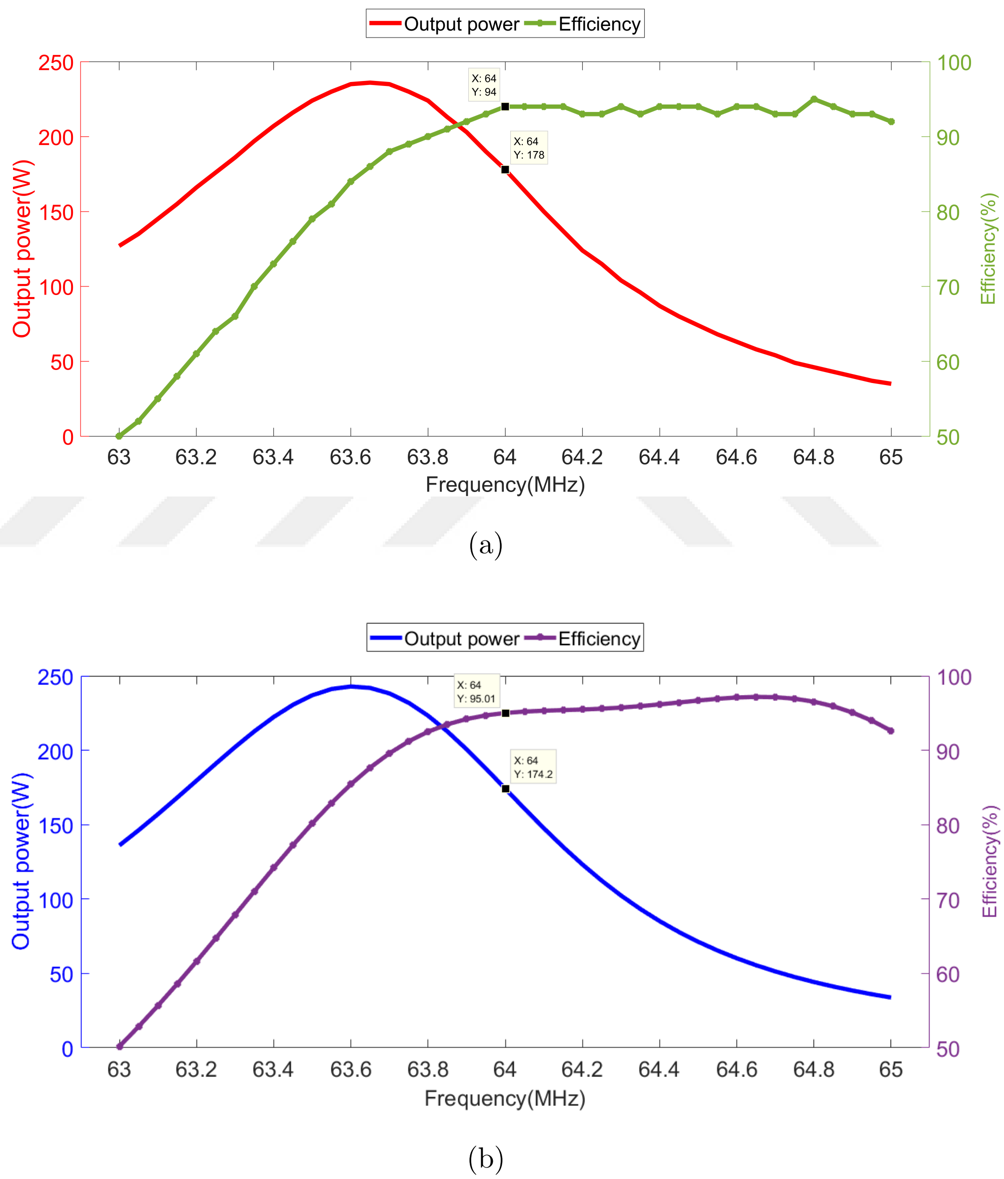

Figure 4.7: Amplifier's frequency response (output power and efficiency). (a) LTSPICE data. (b) The state-space model data.

power and efficiency. In addition, the transient behavior of the sate-space model is analyzed.

4.2.1 State-Space Model

In the first method, the state-space model of class-E amplifiers is simulated in MATLAB by considering the following circuit parameters for the first and the second amplifiers:

R_{L1}=2Ω, L_{s1}=317nH, L_{ch1}=5uH, V_{dc1}=25V, C_{sh1}=130pF, C_{s1}=22pF, period (T)=15.625nsec, and duty cycle=50%

R_{L2}=2Ω, L_{s2}=317nH, L_{ch2}=5uH, V_{dc2}=25V, C_{sh2}=130pF, C_{s2}=22.3pF, period (T)=15.625nsec, and duty cycle=50%.

The effect of the switching transistor's capacitor is also considered as explained in Sec. 4.1.1. The steady-state of the variables for both amplifiers are shown in Fig. 4.8. The total input and output power and the total efficiency of the system are calculated as 342W, 325W, and 95%, respectively.

In the second method, the amplifiers' parameters are selected as:

R_{L1}=R_{L2}=2Ω, L_{s1}=L_{s2}=317nH, L_{ch1}=L_{ch2}=5uH, V_{dc1}=V_{dc2}=25V, C_{sh1}=C_{sh2} =130pF, C_{s1}=C_{s2}=22.17pF, period (T)=15.625nsec, and duty cycle=50%.

In this case, the phase difference of 3.5°, equivalent to 0.15nsec, is set between the amplifiers' signals. The resulting waveforms in steady-state for both amplifiers are illustrated in Fig. 4.9. The total input and output power and the total efficiency of the system are found as 323W, 307W, and 95%, respectively.

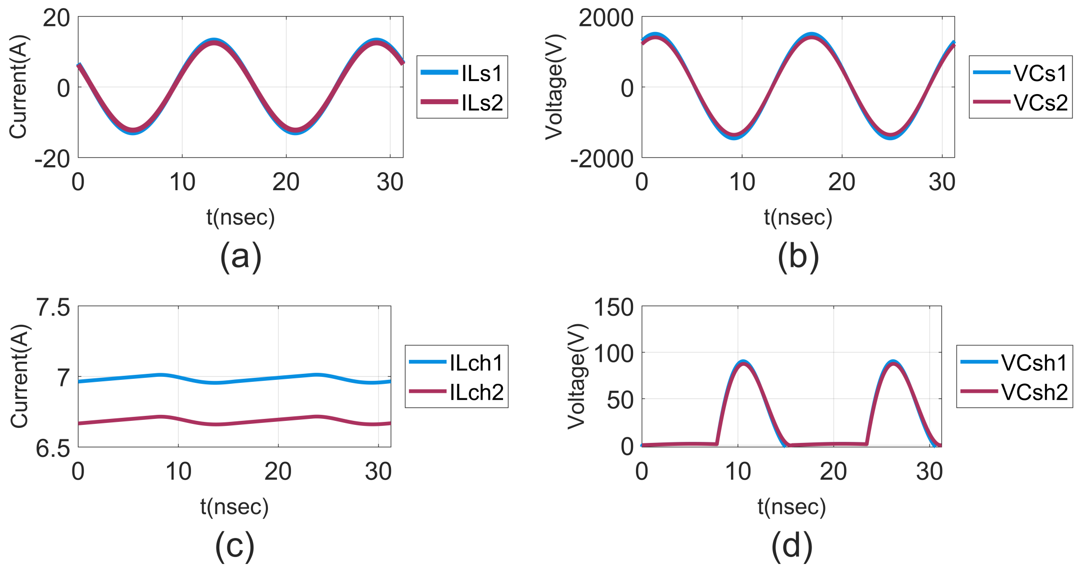

Figure 4.8: Steady-state waveforms of two class-E amplifiers with coupled coils in MATLAB for the first scenario. (a) Series inductors' currents. (b) Series capacitors' voltages. (c) Choke inductors' currents. (d) Shunt capacitors' voltages.

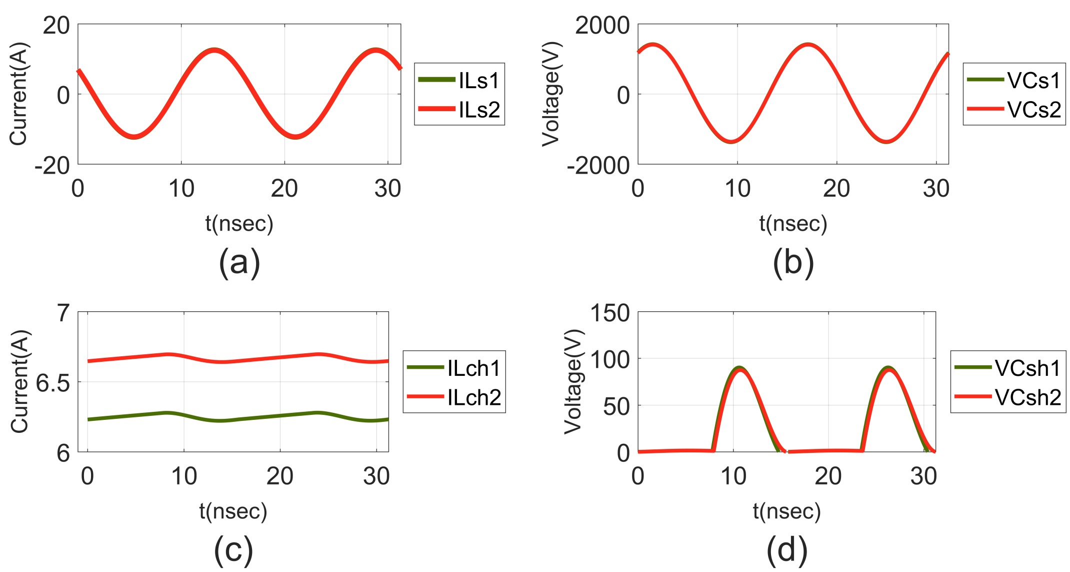

Figure 4.9: Steady-state waveforms of two class-E amplifiers with coupled coils in MATLAB for the second scenario. (a) Series inductors' currents. (b) Series capacitors' voltages. (c) Choke inductors' currents. (d) Shunt capacitors' voltages.

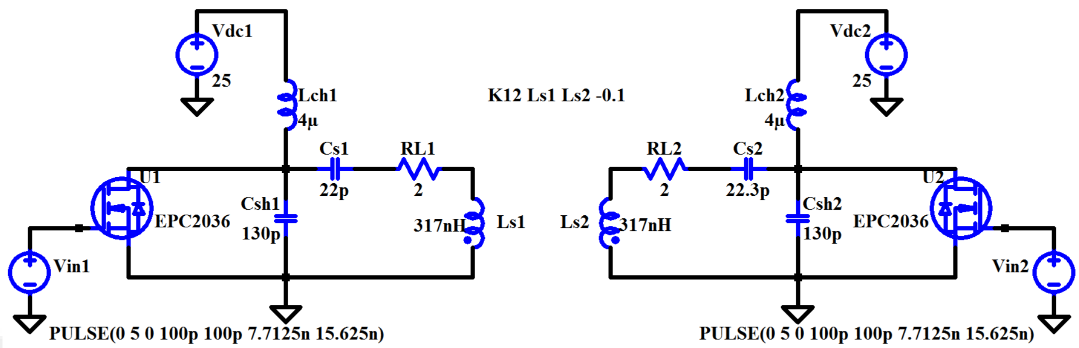

Figure 4.10: Schematic of two class-E amplifiers with coupled coils (the first scenario) in LTSPICE

4.2.2 LTSPICE

The simulation results of the state-space model of two class-E amplifiers with coupled coils are verified in LTSPICE. Figure 4.10 shows the schematic of the amplifiers for the first tuning method. The simulation results are illustrated in Fig. 4.11. The results of the state-space model and LTSPICE are compared in Tab. 4.2. It is observed that the error between the results of these two simulations is not significant.

Following the second tuning method, Fig. 4.12 demonstrates the schematic of the amplifiers with coupled coils. The resulting waveforms are illustrated in Fig. 4.13. A comparison between the results of the state-space model and LTSPICE are given in Tab. 4.3. Similarly, the error between the results of these two simulations is not significant. Therefore, the proposed state-space model represents the behaviors of the system when the coils are coupled and a phase delay is introduced between amplifiers' gate signals.

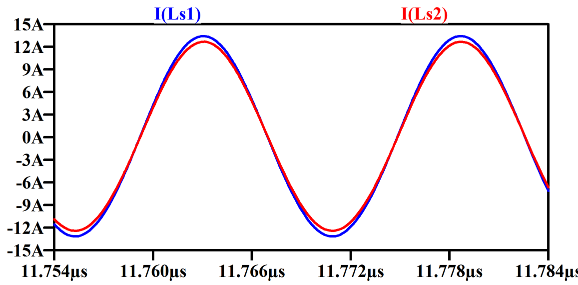

(a)

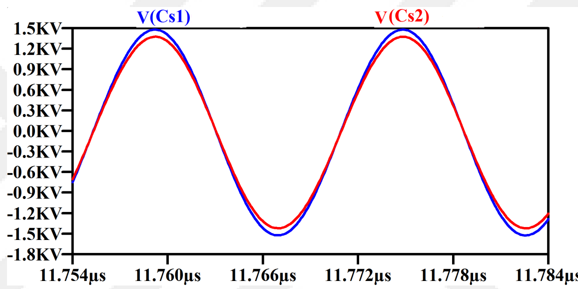

(b)

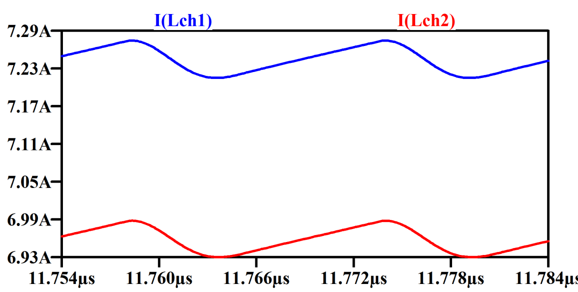

(c)

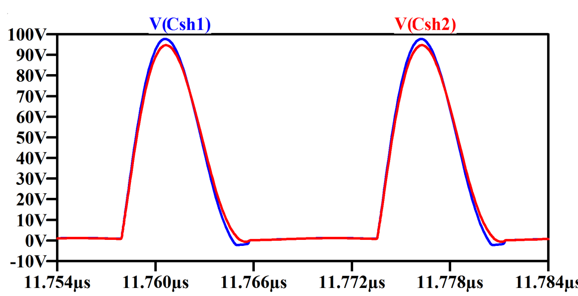

(d)

Figure 4.11: Waveforms of two class-E amplifiers with coupled coils resulting in LTSPICE or the first scenario. (a) Series inductors' currents. (b) Series capacitors' voltages. (c) Choke inductors' currents. (d) Shunt capacitors' voltages.

Parameters	State-space Model	LTSPICE
$I_{L_{ch,1}}$ (average value)	6.9A	7.2A
$V_{C_{sh,1}}$ (peak value)	90.4V	97.7V
$V_{C_{s,1}}$ (peak value)	1506V	1475V
$I_{L_{s,1}}$ (peak value)	13.2A	13.4A
$I_{L_{ch,2}}$ (average value)	6.6A	6.9A
$V_{C_{sh,2}}$ (peak value)	87.4V	94.6V
$V_{C_{s,2}}$ (peak value)	1402V	1375V
$I_{L_{s,2}}$ (peak value)	12.5A	12.6A
Total input power	342W	355W
Total output power	325W	331W
Efficiency	95%	93%

Table 4.2: Comparison of simulation results of the state-space model and LT-SPICE (two class-E amplifiers with coupled coils, the first scenario)

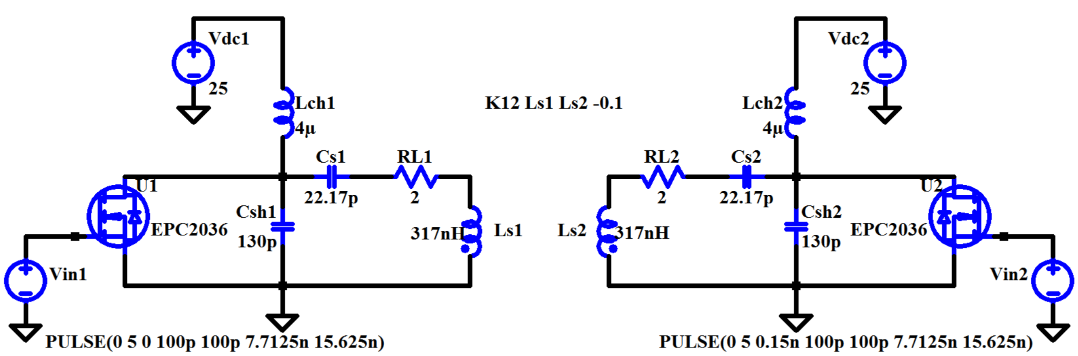

Figure 4.12: Schematic of two class-E amplifiers with coupled coils (the second scenario) in LTSPICE

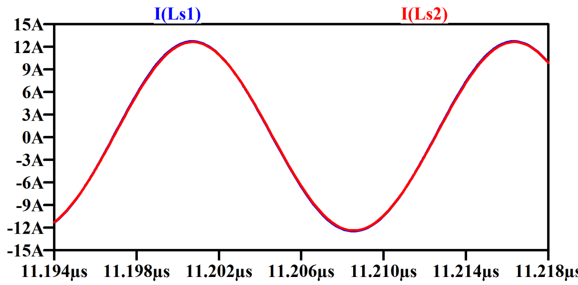

(a)

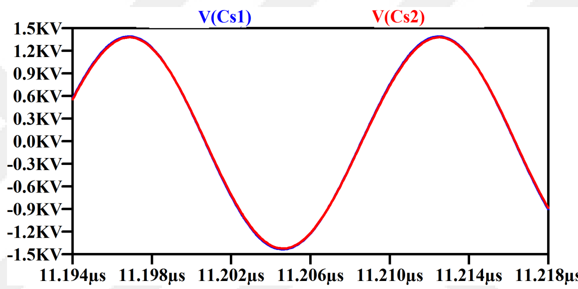

(b)

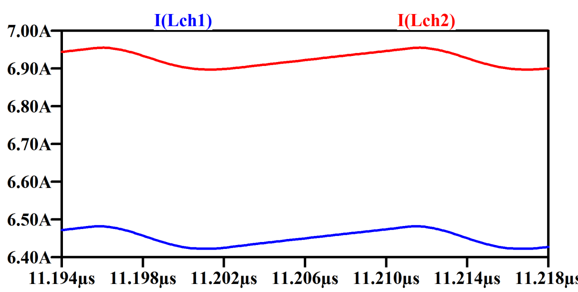

(c)

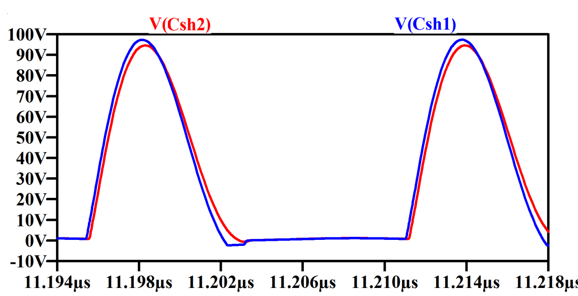

(d)

Figure 4.13: Waveforms of two class-E amplifiers with coupled coils resulting in LTSPICE or the Second scenario. (a) Series inductors' currents. (b) Series capacitors' voltages. (c) Choke inductors' currents. (d) Shunt capacitors' voltages.

Parameters	State-space Model	LTSPICE
$I_{L_{ch,1}}$ (average value)	6.2A	6.5A
$V_{C_{sh,1}}$ (peak value)	90.2V	97.2V
$V_{C_{s,1}}$ (peak value)	1408V	1390V
$I_{L_{s,1}}$ (peak value)	12.5A	12.7A
$I_{L_{ch,2}}$ (average value)	6.7 A	6.9A
$V_{C_{sh,2}}$ (peak value)	87.4V	94.6V
$V_{C_{s,2}}$ (peak value)	1407V	1379V
$I_{L_{s,2}}$ (peak value)	12.4A	12.6A
Total input power	323W	334W
Total output power	307W	314W
Efficiency	95%	94%

Table 4.3: Comparison of simulation results of the state-space model and LT-SPICE (two class-E amplifiers with coupled coils, the second scenario)

4.2.3 Effect of Input Phase Delay and Series Capacitor

In order to achieve high efficiency for two class-E amplifiers with coupled coils, the series capacitor value (C_s) and the phase delay are swept from 21.5pF to 23.5pF and from 0° to 360°, respectively, as illustrated in Fig. 4.14. It is observed in Fig. 4.14 that the efficiency is high enough for some parts of C_s and phase delay values' ranges. In addition to the efficiency, the output power are also required to be considered at the same time due to the maximum power limitation (450W) of the system. The output power with respect to C_s and phase delay values are shown in Fig. 4.15. Considering these figures and the limitations, the values of C_s and phase delay can be found for high efficiency operation of the class-E amplifiers. Switches waveforms (V_{Csh1} and V_{Csh2}) are shown in Fig. 4.16 for different values of C_s and phase delay. These values are selected using Fig. 4.14 and Fig. 4.15. The obtained C_s value is the same for both amplifiers. It should be noted that the amplifiers are similar except the phase delay between their gate signals.

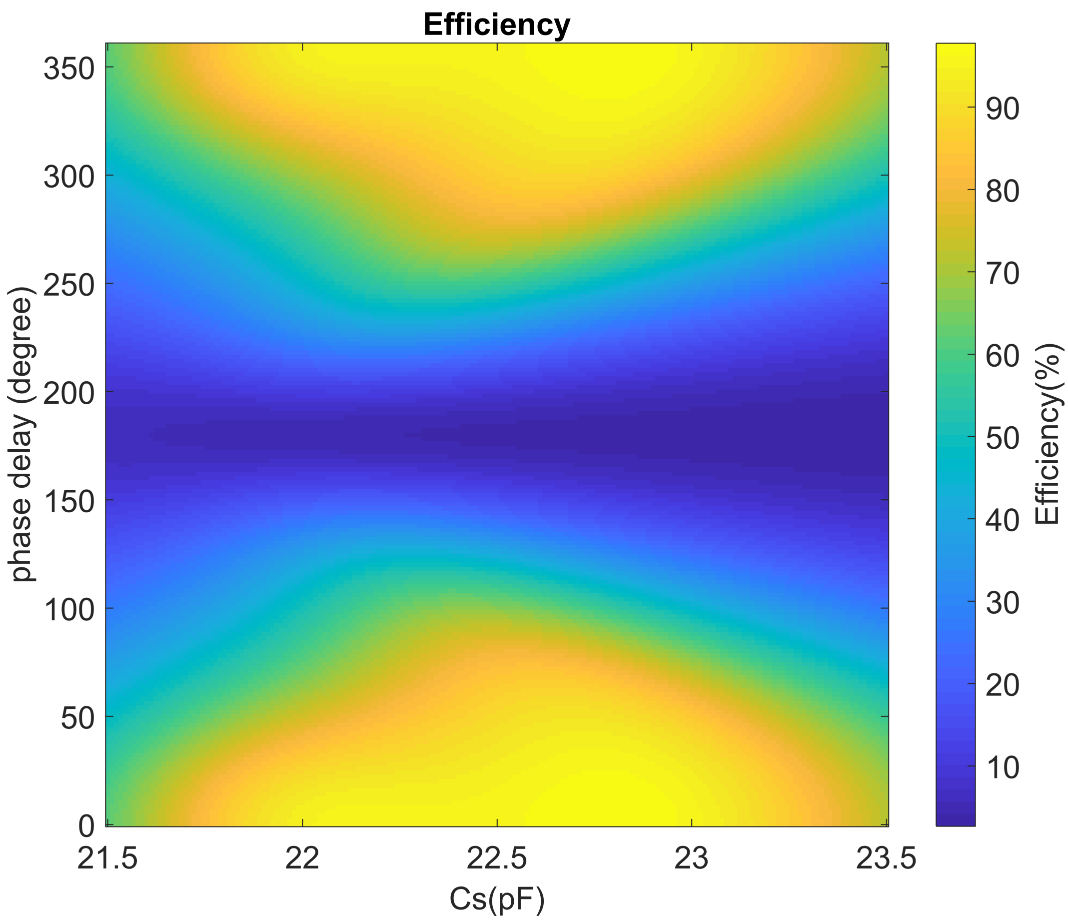

Figure 4.14: Efficiency of two class-E amplifiers with coupled coils regarding series (C_s) capacitor values and phase delays

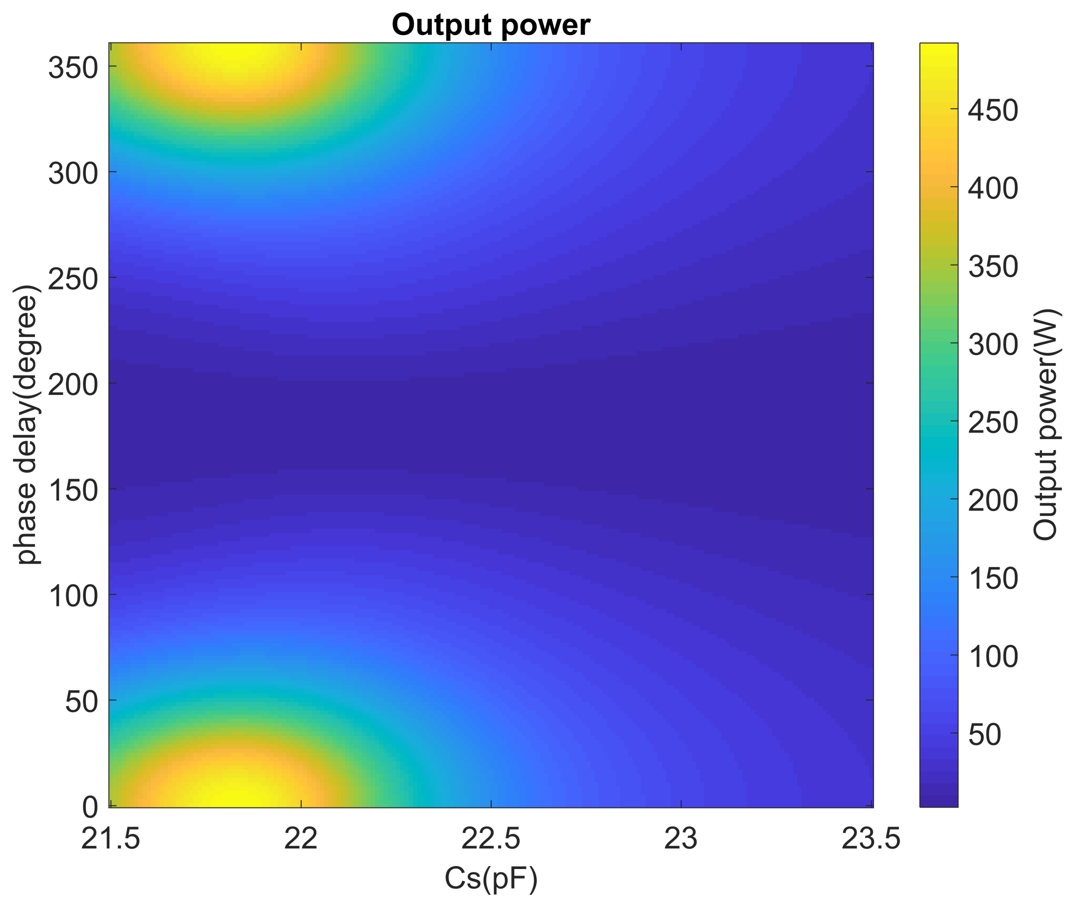

Figure 4.15: Output power of two class-E amplifiers with coupled coils regarding series (C_s) capacitor values and phase delays

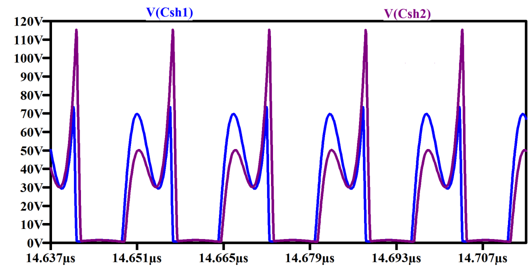

(a) C_s=21.59pF, phase=10°, leading to P_{out}=580W, η=68%.

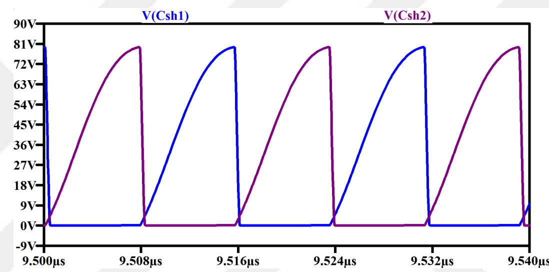

(b) C_s=21.81pF, phase=180°, leading to P_{out}=4.1W, η=5%.

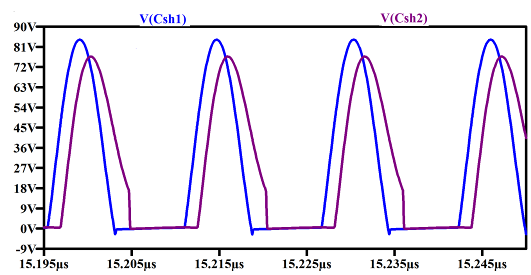

(c) C_s=22.7pF, phase=34°, leading to P_{out}=88W, η=95%.

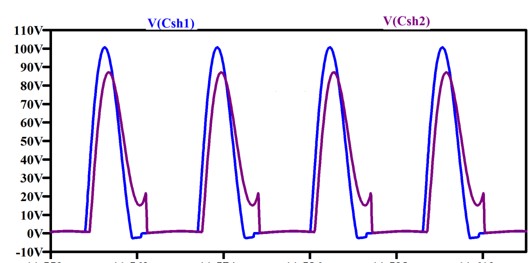

(d) C_s=22.1pF, phase=14°, leading to P_{out}=358W, η=94%.

Figure 4.16: Switches' waveforms of two class-E amplifiers with coupled coils at different selected C_s and phase delay values. The output power (P_{out}) and efficiency (η) are found using Fig. 4.14 and Fig. 4.15.

4.2.4 Transient Analysis and Frequency Response of the System

Since class-E amplifiers are controlled digitally by changing gates' signals and supply modulations, it is important that the dynamics of the sampled-data system (Eq. 2.62) reaches its steady-state as fast as possible. To this end, it is required to reduce the time constant of the system.

Using the mathematical results of Sec. 2.4, the transient behavior of two class-E amplifiers with coupled coils is analyzed. This is done by investigating the state-space model and finding its eigenvalues which are dependent on the phase delay and C_s values (see Eq. 2.49, 2.56 and 2.63). The time constant of the system with respect to C_s and phase delay is illustrated in Fig. 4.17. It is seen that for the whole range of phase delay and C_s variations, the time constant remains less than 2.2μsec for the specified values of phase delay and C_s.

For the two class-E amplifiers with coupled coils (see Fig. 4.12), output power and efficiency with respect to frequency changes are illustrated in Fig. 4.18 and Fig. 4.19, respectively. It is seen that the system's efficiency and power are highly dependent on the phase delay between the amplifiers for the range of frequencies around 64MHz.

4.3 Three Class-E Amplifiers with Significantly Coupled Coils

The reliability of the proposed state-space model has been analyzed and demonstrated in the previous sections. In this section, three similar class-E amplifiers are considered when the coils are significantly coupled ($k_{12} = k_{13} = -0.1$). The amplifiers' parameters are assumed as follows

R_{L1}=R_{L2}=R_{L3}=2Ω, L_{s1}=L_{s2}=L_{s3}=317nH, L_{ch1}=L_{ch2}=L_{ch3}=5uH, V_{dc1}=V_{dc2}=

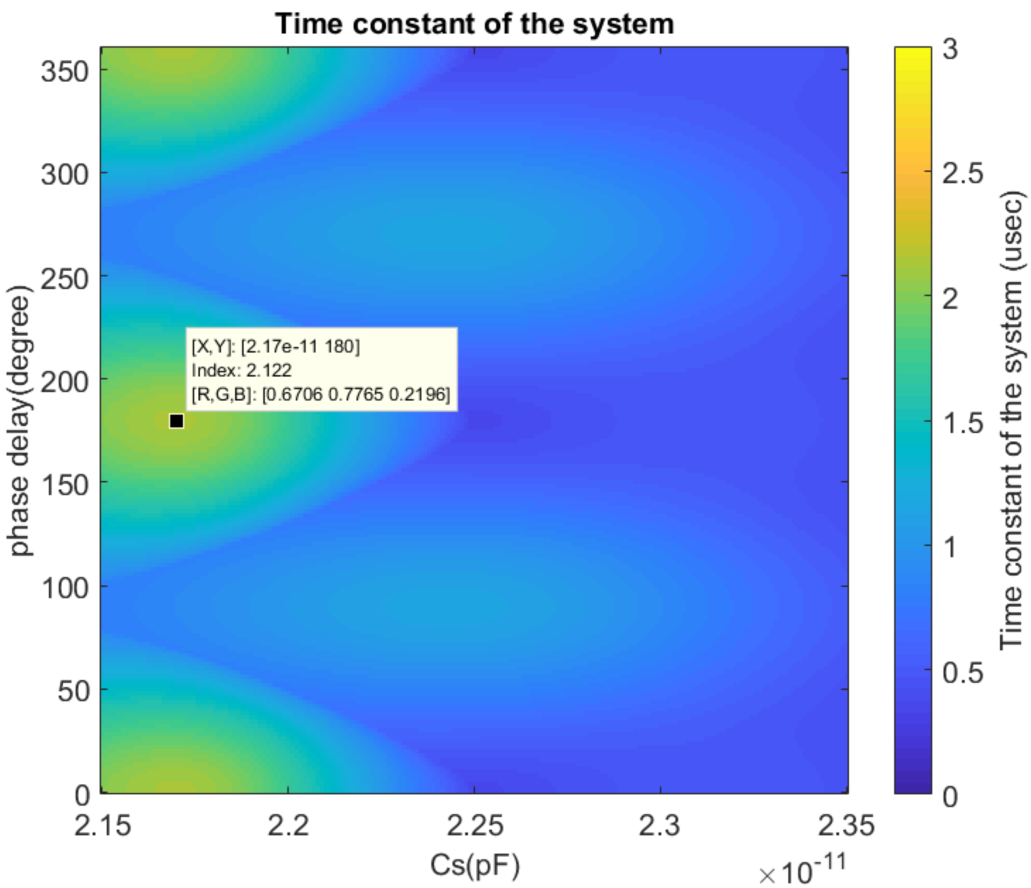

Figure 4.17: Time constant of the system with respect to C_s and phase delay

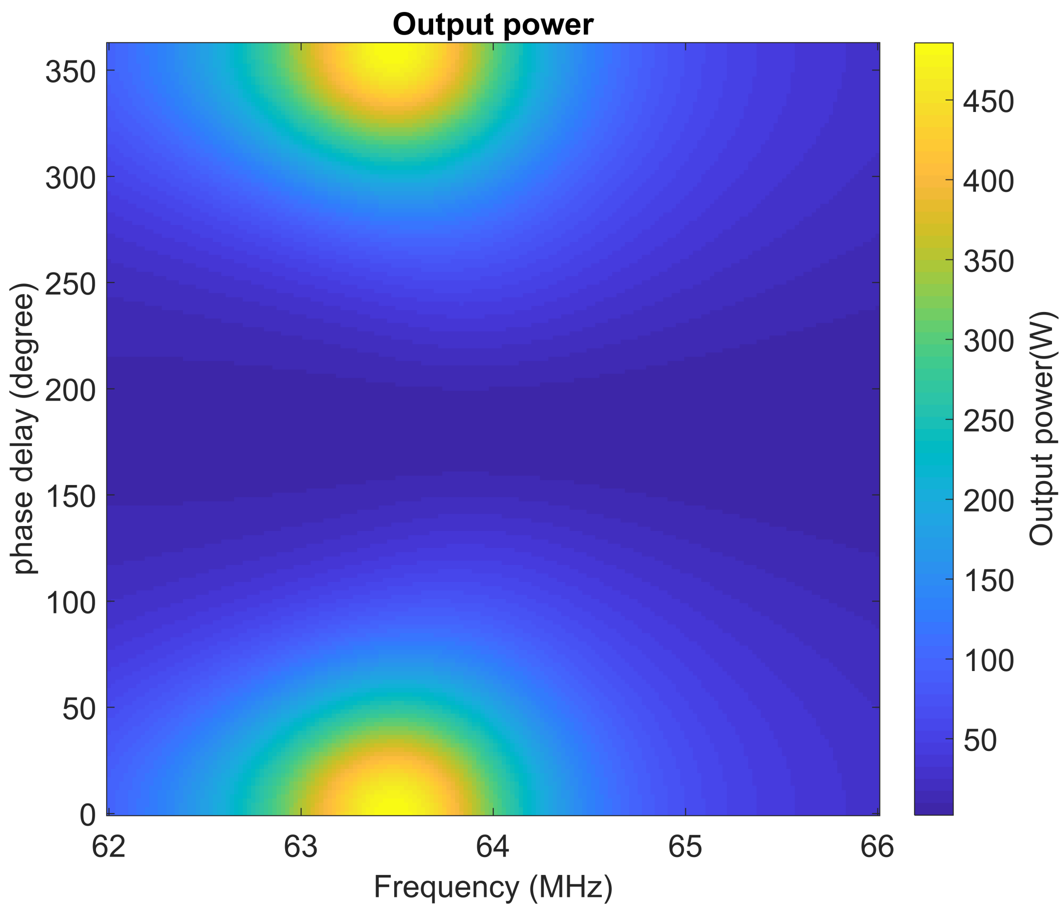

Figure 4.18: Output power of two class-E amplifiers with coupled coils regarding to frequency and phase delay variations

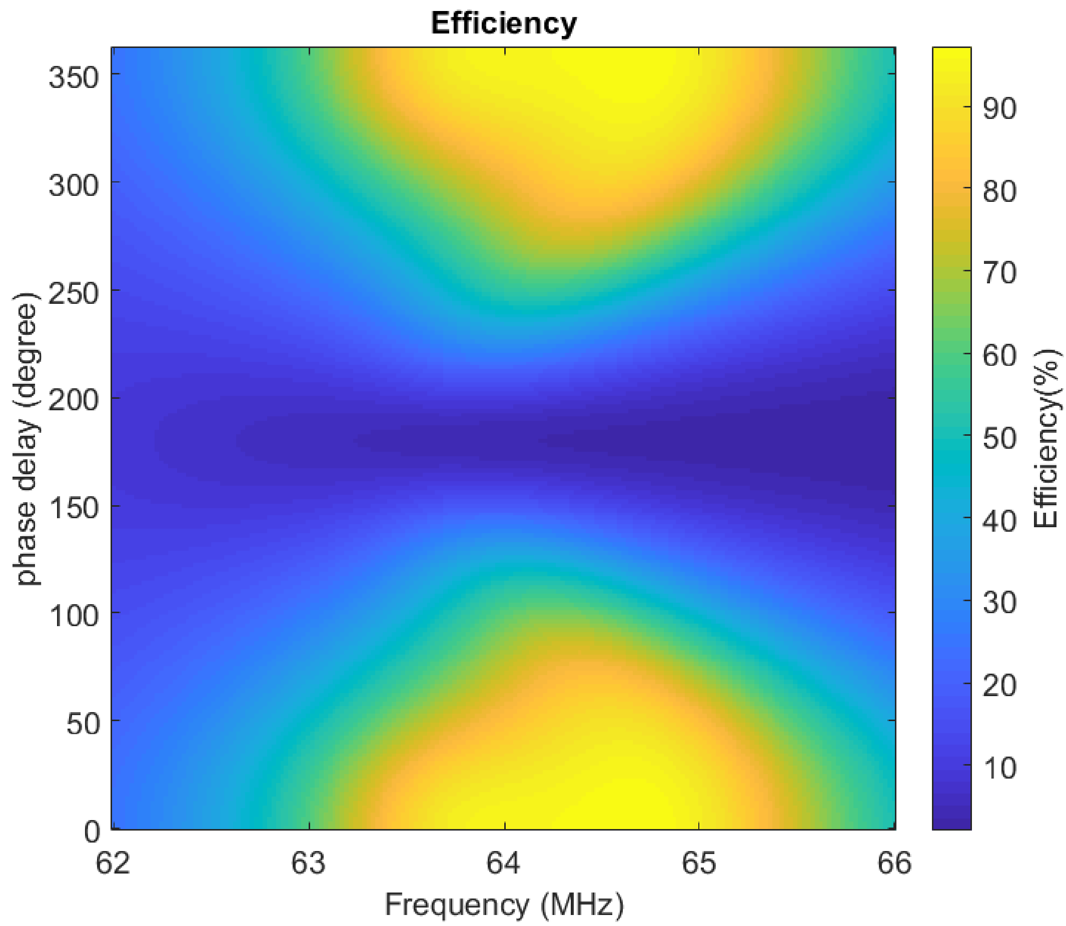

Figure 4.19: Efficiency of two class-E amplifiers with coupled coils regarding to frequency and phase delay variations

V_{dc3}=25V, C_{sh1}=C_{sh2}=C_{sh3} =130pF, C_{s1}=C_{s2}=C_{s2}=25pF, period (T)=15.625nsec, and duty cycle=50%.

In the following, the effect of phase delays between the amplifiers are investigated to achieve high output power and high efficiency. In addition, the transient behavior of the sate-space model is analyzed.

4.3.1 Effect of Input Phase Delays Variations

In order to achieve high efficiency for three class-E amplifiers with coupled coils, the phase delays between channels 1&2 and 1&3 are swept from 0° to 360° as illustrated in Fig. 4.20. It is seen in Fig. 4.20 that the efficiency is relatively high for different phase delays' ranges. In addition to the efficiency, the output power is also required to be considered at the same time. The output power with respect to the phase delays between channels 1&2 and 1&3 is demonstrated in Fig. 4.21. Considering these figures and the limitations, the values of the phase delays can be found for the high efficiency operation modes of the class-E amplifiers. Switches waveforms (V_{Csh1}, V_{Csh2}, and V_{Csh3}) are shown in Fig. 4.22 for different values of phase delays between channels 1&2 and 1&3. These values are selected using Fig. 4.20 and Fig. 4.21.

4.3.2 Transient Analysis of the System

The transient behavior of three class-E amplifiers with coupled coils is analyzed. The time constant of the system with respect to phase delays between channels 1&2 and 1&3 is illustrated in Fig. 4.23. It is observed that for the whole range of phase delays, the time constant remains less than 1μsec for the specified values of phase delays.

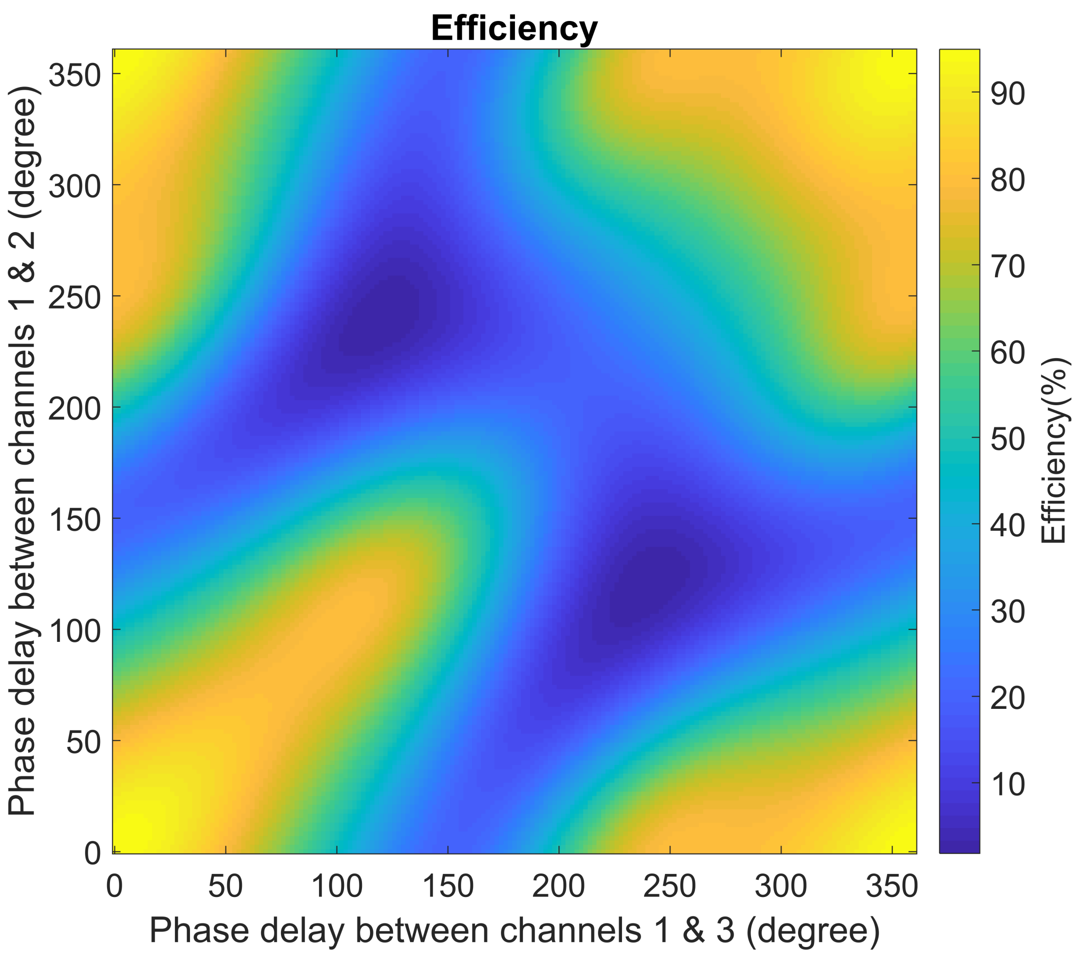

Figure 4.20: Efficiency of three class-E amplifiers with coupled coils regarding phase delays between channels 1&2 and 1&3

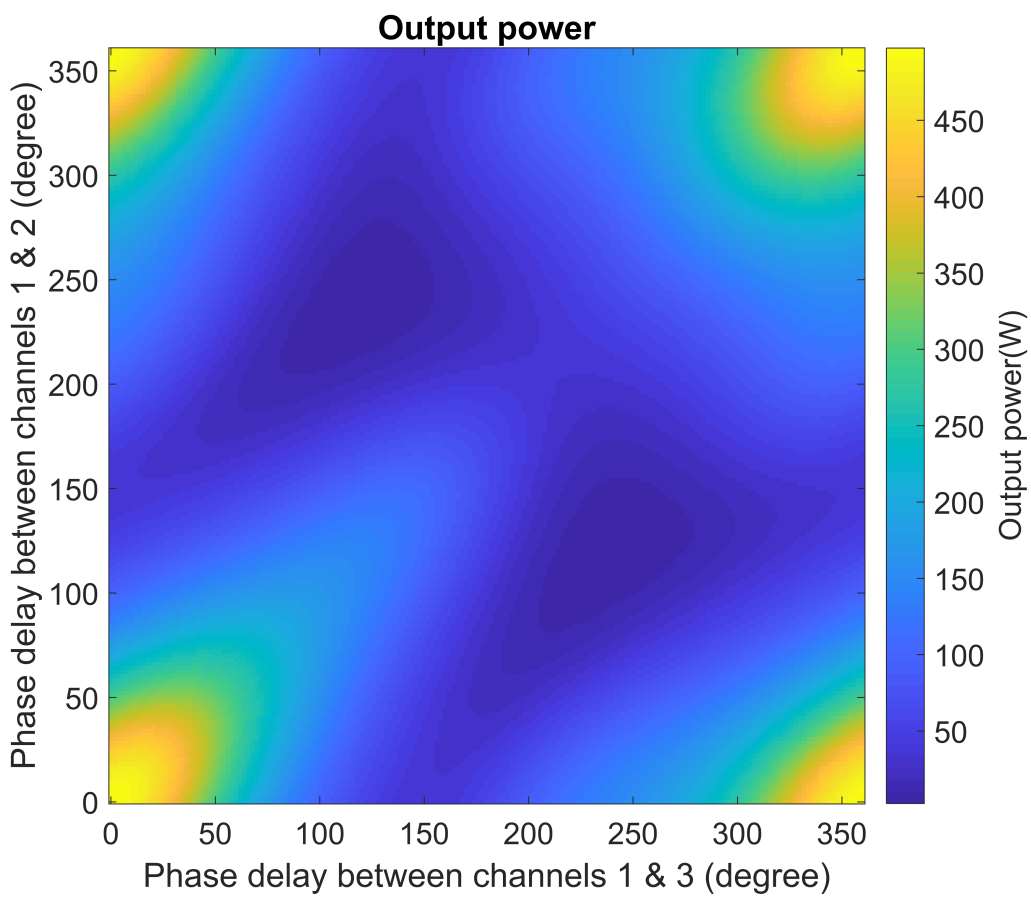

Figure 4.21: Output power of three class-E amplifiers with coupled coils regarding phase delays between channels 1&2 and 1&3

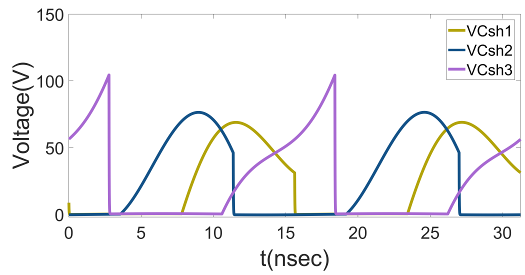

(a) $\Delta\Phi_{1\&2}$=262°, $\Delta\Phi_{1\&3}$=64°, P_{out}=64W, η=41%.

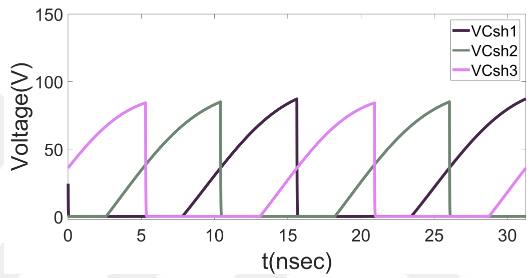

(b) $\Delta\Phi_{1\&2}$=240°, $\Delta\Phi_{1\&3}$=122°, P_{out}=3W, η=2%.

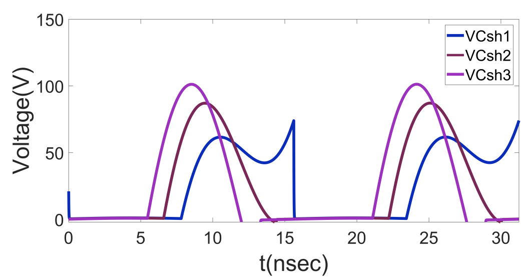

(c) $\Delta\Phi_{1\&2}$=332°, $\Delta\Phi_{1\&3}$=306°, P_{out}=322W, η=82%.

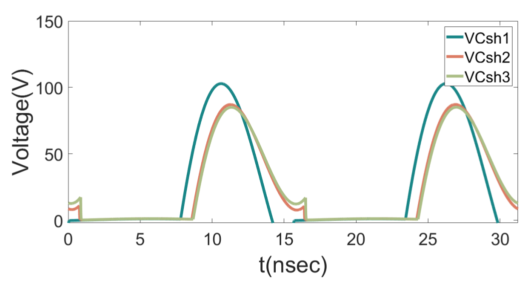

(d) $\Delta\Phi_{1\&2}$=18°, $\Delta\Phi_{1\&3}$=20°, P_{out}=463W, η=92%.

Figure 4.22: Switches' waveforms of three class-E amplifiers with coupled coils at different selected phase delay values between channels 1&2 ($\Delta\Phi_{1\&2}$) and 1&3 ($\Delta\Phi_{1\&3}$). The output power (P_{out}) and efficiency (η) are found using Fig. 4.21 and Fig. 4.20

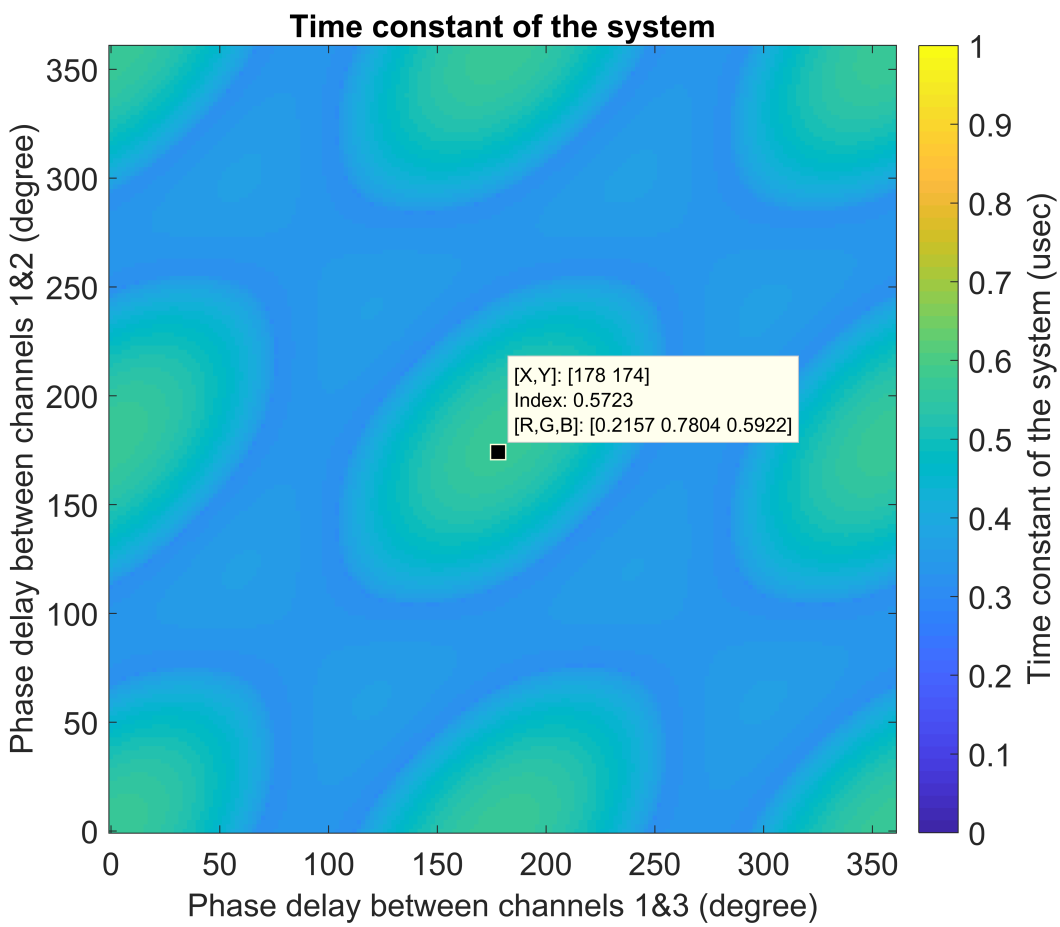

Figure 4.23: Time constant of the system with respect to phase delays between channels 1&2 and 1&3

4.4 Driver and Supply Modulation Simulation Results

The amplifier's circuit is simulated in ADS and LTSPICE as explained in Sec. 3.2.3. The values of resistors and capacitors are chosen according to the design requirements. Figures 4.24 and 4.25 show the driver's circuit signals in ADS and LTSPICE, respectively. The rise and fall times of the driver signal are found in ADS as 750psec and 780psec, and in LTSPICE as 980psec and 870psec. The error between the rise and fall times in these two simulations may be due to the simulation resolution, numerical errors, and some component mismatches. It is also seen that the amplitude of the driver signal is 4.9V in both simulations. Considering these results, it can be concluded that the driver circuit operates properly since the rise and fall times are found less than 1nsec, and the amplitude remains around 5V as expected.

Figures 4.26 and 4.27 illustrate supply modulation signals generated in ADS and LTSPICE, respectively. It is noted that the supply voltage of 7.5V is applied and the duty cycle of 90% is considered for the 1MHz signal in these figures. There is a negligible error between the results of these two simulations. This validates that the supply modulation circuit works properly.

4.5 Driver and Supply Modulation Experimental Results

This section provides the experimental results of the implemented amplifier. The signals are measured using an active probe N2796A (Agilent). Figure 4.28 shows the driver signals. The rise and fall times, and the amplitude of the driver output are measured. The experimental and simulation results are compared in Tab. 4.4. It is observed that the experimental results are pretty similar to the simulation results. As expected, the rise and fall times are not greater than 1nsec.

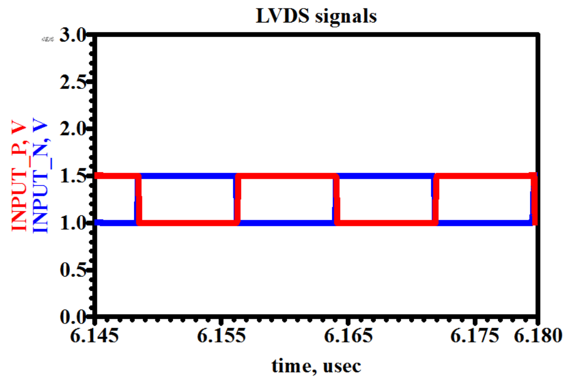

(a)

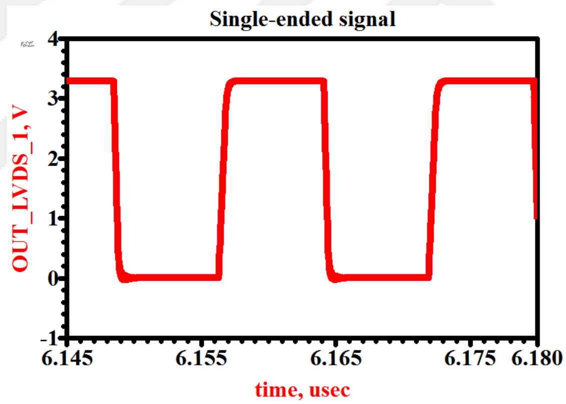

(b)

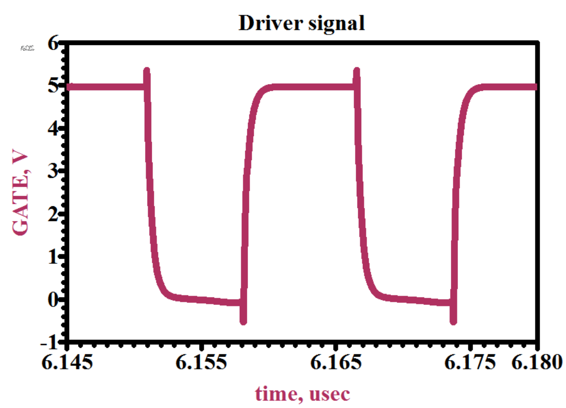

(c)

Figure 4.24: Driver simulation results in ADS. (a) LVDS signals. (b) Single-ended signal. (c) Driver's output signal.

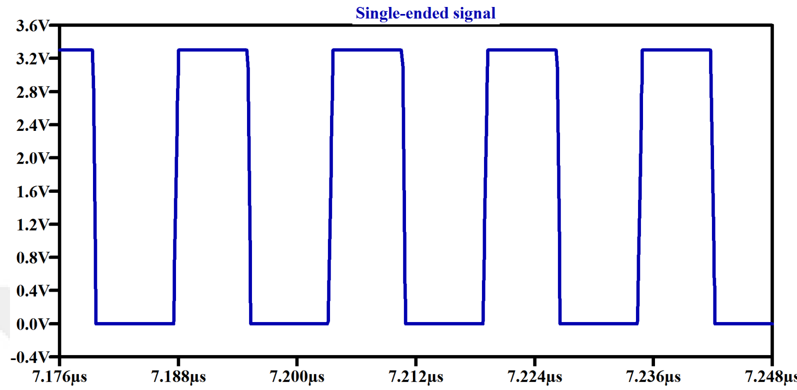

(a)

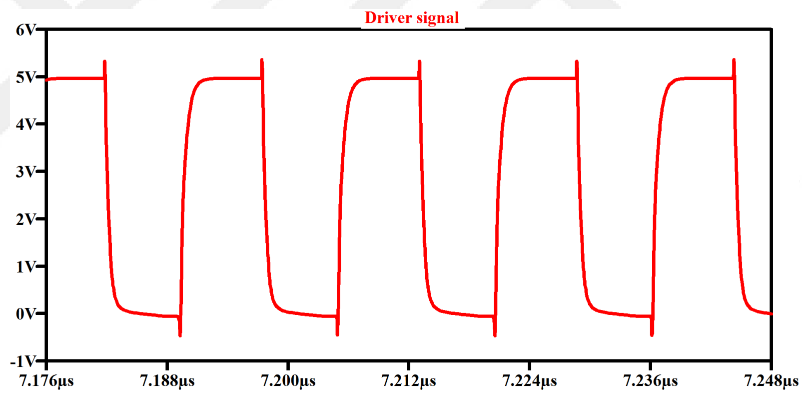

(b)

Figure 4.25: Driver simulation results in LTSPICE. (a) Single-ended signal. (b) Driver's output signal

Parameters	Simulation		Experimental
	LTSPICE	ADS	
Rise time (ps)	980	750	1000
Fall time (ps)	870	780	840
Amplitude (V)	4.9	4.9	4.6

Table 4.4: Comparison of the experimental and simulation results for the driver output

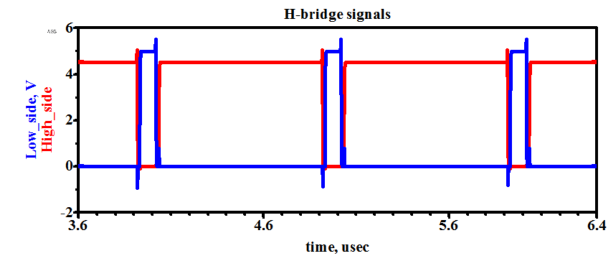

(a)

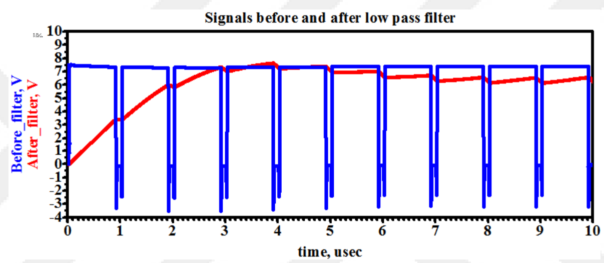

(b)

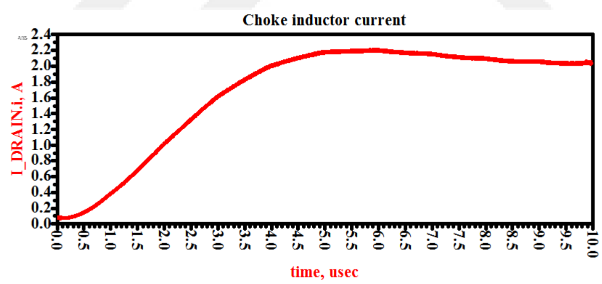

(c)

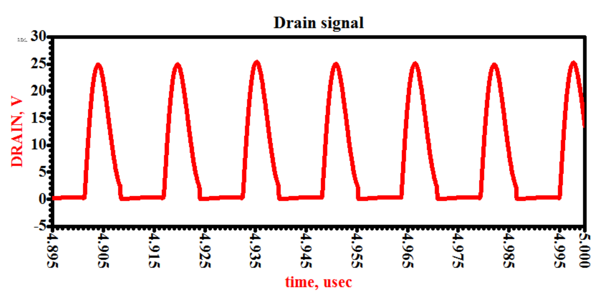

(d)

Figure 4.26: Supply modulation simulation results in ADS. (a) High-side and low-side input signals of H-bridge (EPC2106). (b) H-bridge's output with and without low-pass filter. (c) Choke inductor current. (d) Drain voltage of the switching transistor.

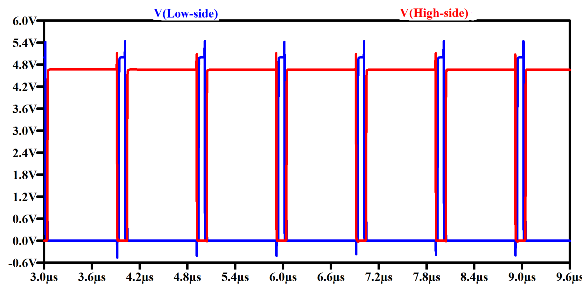

(a)

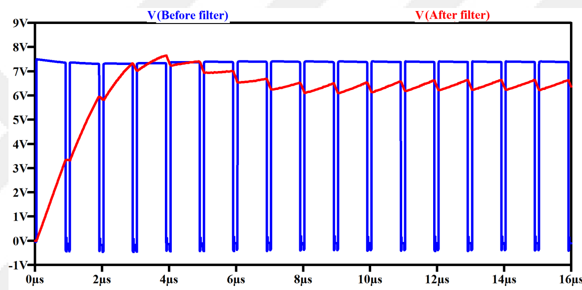

(b)

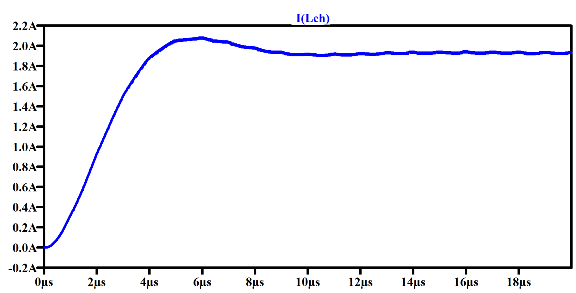

(c)

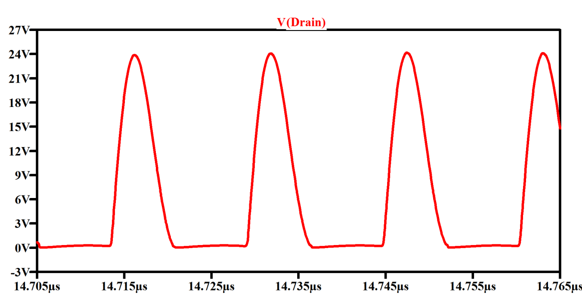

(d)

Figure 4.27: Supply modulation simulation results in LTSPICE. (a) High-side and low-side input signals of H-bridge (EPC2106). (b) H-bridge's output with and without low-pass filter. (c) Choke inductor current. (d) Drain voltage.

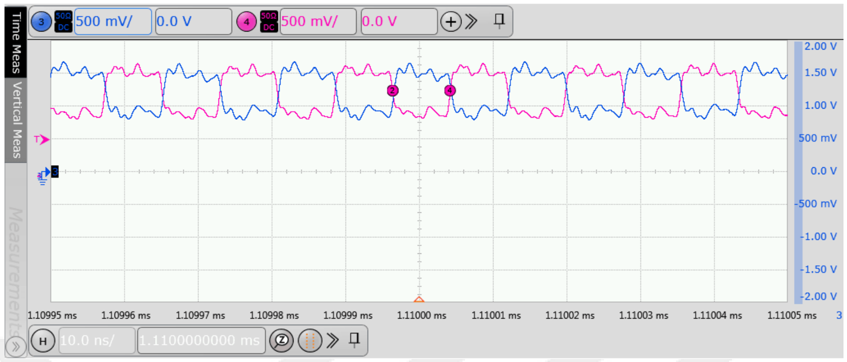

(a)

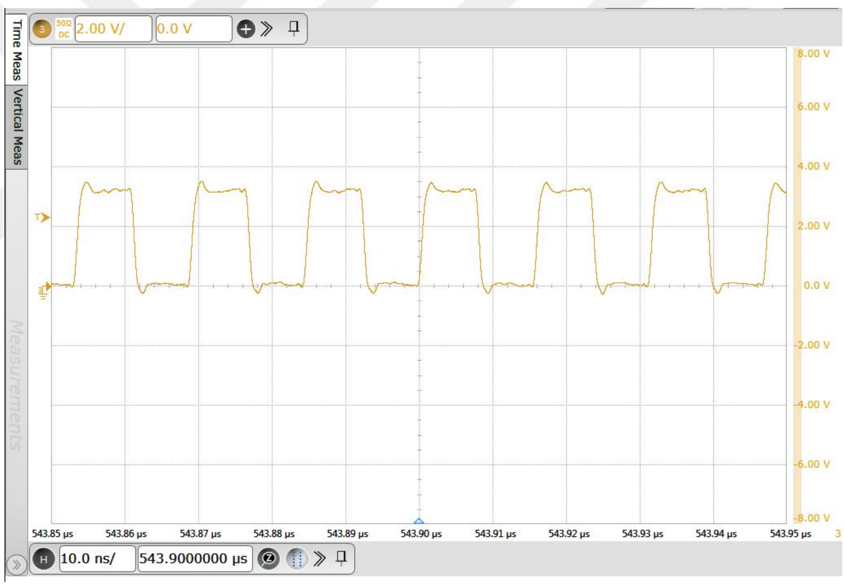

(b)

(c)

Figure 4.28: Driver measurement results. (a) LVDS signals from FPGA. (b) Single-ended signal. (c) Driver's output signal (gate signal of EPC2036)

Two air core inductors, 2uH and 4uH, are made for the low-pass filter and the choke inductor. To reduce the coupling between these two inductors, they are placed perpendicular to each other on the PCB (see Fig. 3.9). A 2msec sinc envelope is also applied for the supply modulation. Using this envelope, the duty cycle of the 1MHz signal varies between 5% and 95% (see Sec. 2.4.2). Figure 4.29 illustrates supply modulation signals. The current through the choke inductor is measured using a current probe 1146B (Agilent). The series and shunt capacitors are tuned, and the drain voltage of the transistor (EPC2036) is shown in Fig. 4.30. By comparing the experiment and simulation results, it can be seen the supply modulation circuit provides correct outputs. However, the drain voltage of the transistor in the experiment is slightly less than its value in the simulation. This difference is due to the measurement errors and using non-ideal components.

4.6 Power and Efficiency Measurement Results

The experimental setup explained in Sec. 3.3 is used to measure the amplifier's power and efficiency. The amplifier is connected to the RF coil loaded with a phantom. Before performing power and efficiency measurements, the series and shunt capacitors are tuned using the estimated values in the simulations. It should be noted that these estimated values may be readjusted when tuning the amplifier in the experiment. This adjustment is due to the measurement errors and using non-ideal components. The pick-up coil's signal, when the supply voltage is set to 12V, is shown in Fig. 4.31.

Considering the peak amplitude of the pick-up coil signal, shown in Fig. 4.31, and α=500, the output power is calculated. The input power is also calculated by measuring the supply current. Using the input and output powers, efficiency can be found. The experimental and simulation results are provided in Tab. 4.5. It can be observed that the efficiency of the state-space model and LT-SPICE are almost similar, however, there is a difference between their power level resulting from the effect the shunt capacitor and on-resistance values approximation in MATLAB. It is also seen that the input power level in LTSPICE

(a)

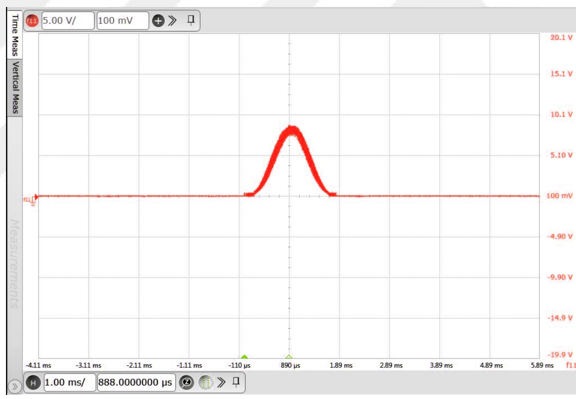

(b)

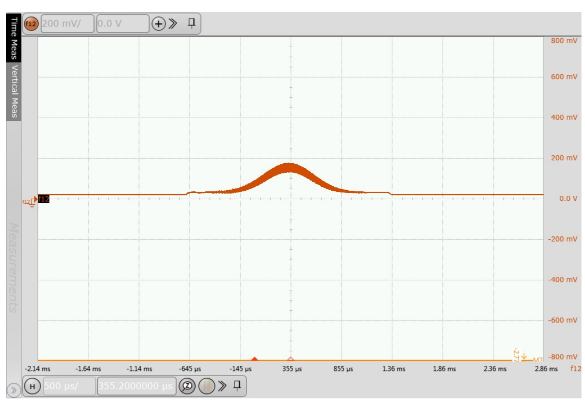

(c)

Figure 4.29: Supply modulation measurement results. (a) High-side (pink) and low-side (blue) input signals of H-bridge when the duty cycle is about 60%. (b) Output of the supply modulation. (c) Choke inductor current profile.

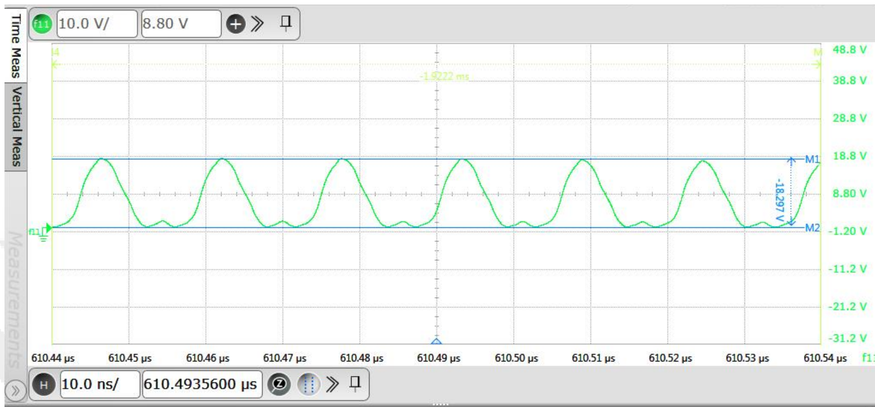

Figure 4.30: Drain voltage of the transistor (EPC2036)

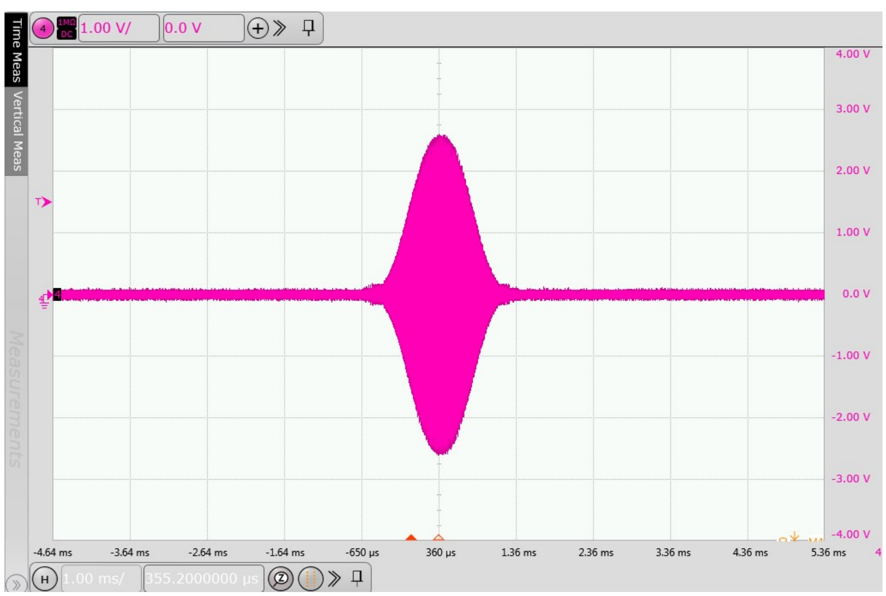

Figure 4.31: Output voltage of the pick-up coil

	Input power (W)	Output power (W)	Efficiency (%)
State-space model	38	36	95
LTSPICE	37	35	94
ADS	37	30	81
Experiment	30	24	80

Table 4.5: Comparison of the input and output power, and the efficiency in the experiment and simulations

and ADS are similar while their output power levels are different, which leads to different efficiencies. The main reason is that the series and shunt capacitors are not well-tuned in ADS (see Fig. 4.26d). The experimental results show a proper consistency with state-space and simulation results. The power levels of the experimental results are lower since the non-ideal components are employed. Furthermore, measurement errors and imperfect tuning are the other reasons for non-identical experimental and simulation results.

Chapter 5

Discussion and Conclusion

This thesis proposes a state-space model for an array of on-coil class-E amplifiers considering switches' on-resistance and coupling effects between the coils. For a single class-E amplifier, this is done by employing and solving the state equations in both on and off switching conditions. Then, the state-space model is extended for an array of class-E amplifiers with coupled coils. By having an array of class-E amplifiers with coupled coils, instead of only two conditions (on and off), various combinations of switches' conditions should be considered, complicating the analysis. However, using the state-space simplifies the analysis and provides an insight into each state's behavior. In addition, employing the state-space model shows that the input and output powers can be calculated using the initial conditions. Moreover, the state-space model provides a simulation setup to investigate the effects of applying different phase delays between the gate signals of the amplifiers. The sampled-data system generated from the state-space model equips the designer with a powerful tool for analyzing the transient behavior by investigating the time constant of the system.

In addition, novel hardware is also designed for the class-E amplifier. In this design, the goal is to retain high efficiency while reducing the size of the PCB and price. The required number of amplifiers increases to provide enough power in the transmit system. Therefore, the size of the PCB is crucial due to the lack of space inside the scanner's bore. To this end, the previous PCB is redesigned to be almost half the size of the previous one. Also, the number of DC voltage inputs is reduced to one, resulting in a cost-efficient design with less cabling requirement. The driver, controlled by an FPGA, is designed to keep its rise and fall times less than 1nsec. The Gallium Nitride (GaN) power FET, EPC2036, is selected as the switching transistor in this design. It has low on-resistance (R_{dson} =73mΩ), and its maximum drain to source voltage is 100V. The other advantages of EPC2036 are its small size (0.9mm$\times$0.9mm) that shrinks the PCB size, and its low price, which leads to a cost-efficient final product. The final cost of the amplifier, including manufacturing PCB and its components, is approximately 190 US dollars.

The simulations are performed for a single class-E amplifier and two class-E amplifiers with coupled coils in MATLAB and LTSPICE. The state variables' waveforms, input and output powers, and efficiency are compared in both simulations for a single class-E amplifier. It is shown that the results are pretty close. Numerical values of input and output powers and efficiency are calculated for both the state-space model and LTSPICE. It is reported that the difference between the results of the state-space model and LTSPICE is less than 3% for input and output powers, and efficiency. The reason for this small error is that the estimated values of the transistor's capacitor (C_{ds}) and on-resistor (R_{dson}) are used in MATLAB simulations. In addition, MATLAB generates an ideal pulse as a gate signal, while in the LTSPICE, the gate signal is not an ideal pulse, and its rise and fall times are 100psec, which may also affect the simulation results. Deviations of efficiency and output power with respect to series (C_s) and shunt (C_{sh}) capacitors' values are illustrated. It is demonstrated that the efficiency is high for most of the range of change of (C_s) and (C_{sh}). However, it is observed that the pair of (C_s) and (C_{sh}) values that leads to high efficiency may result in low or impractical output power. In practice, due to the maximum transistor's voltage limit (V_{dsmax}) and its current (I_D), the output power is also limited, and its associated (C_s) and (C_{sh}) values should not be utilized even if they lead to high efficiency.

The simulation results of two class-E amplifiers with coupled coils are also compared in MATLAB and LTSPICE for two scenarios. The state variables' waveforms, input and output powers, and efficiency are compared in both simulations. It is shown that the results are pretty close. Numerical values of input and output powers and efficiency are calculated for both the state-space model and LTSPICE. It is reported that the difference between the results of the state-space model and LTSPICE is less than 3% for input and output powers, and efficiency. The reason for this small error is that the estimated values of the transistor's capacitor (C_{ds}) and on-resistor (R_{dson}) are used in MATLAB simulations. In addition, MATLAB generates an ideal pulse as a gate signal, while in the LTSPICE, the gate signal is not an ideal pulse, and its rise and fall times are 100psec, which may also affect the simulation results. Deviations of efficiency and output power with respect to series (C_s) and shunt (C_{sh}) capacitors' values are illustrated. It is demonstrated that the efficiency is high for most of the range of (C_s) and (C_{sh}) values. However, it is observed that the pair of (C_s) and (C_{sh}) values that leads to high efficiency may result in low or impractical output power. In practice, due to the maximum transistor's voltage limit (V_{dsmax}), the output power is also limited, and its associated (C_s) and (C_{sh}) values should not be utilized even if they lead to high efficiency.

The simulation results of two class-E amplifiers with significantly coupled coils are also compared in MATLAB and LTSPICE for two different scenarios. The first scenario shows that the system can achieve high output power and efficiency by adjusting only series capacitor values (C_{s1} and C_{s2}). In the second scenario, high output and efficiency are achieved by introducing a phase delay to the gate signal of the second amplifier. Numerical values of input and output powers and efficiency are calculated for both the state-space model and LTSPICE. It is reported that the error between the state-space model and LTSPICE results is less than 3% for input and output powers, and efficiency in both scenarios. Then, the efficiency and output power of the system with respect to series (C_s) capacitor value and phase delays are shown. According to the results, the efficiency is high for some of the range of C_s values and phase delays. However, practical limits on output power should be considered for choosing the C_s value and phase delay. Also, the efficiency and output power of three class-E amplifiers with significantly coupled coils are plotted with respect to phase delays between channels 1&2 and

1&3. It is shown that some modes of operation exist where the efficiency is high and the output power is in the practical range.

After implementing the designed amplifier and testing the PCB, the power and efficiency are measured and compared to the simulation results. It is shown that the amplifier can achieve 24W output power and 80% efficiency when the supply voltage is 12V. The experimental results have a proper consistency with state-space and simulation results.

For future work, the current approach is going to be investigated by performing experiments on more amplifiers with coupled coils. The effect of phase delays is currently considered on up to three amplifiers. The other research direction for the future is to analyze the phase delays effect for a higher number of amplifiers in the system. In addition to phase delays, the impact of other parameters like input amplitude may also need to be taken into consideration.

Bibliography

[1] G. Katti, S. A. Ara, and A. Shireen, “Magnetic Resonance Imaging (MRI)-A Review,” *International Journal of Dental Clinics*, vol. 3, no. 1, pp. 65–70, 2011.

[2] J. C. Richardson, R. W. Bowtell, K. Mäder, and C. D. Melia, “Pharmaceutical Applications of Magnetic Resonance Imaging (MRI),” *Advanced Drug Delivery Reviews*, vol. 57, no. 8, pp. 1191–1209, 2005.

[3] Q. Wang, “Hardware of MRI System,” in *Nuclear Magnetic Resonance*, IntechOpen, 2019.

[4] E. Moser, A. Stadlbauer, C. Windischberger, H. H. Quick, and M. E. Ladd, “Magnetic Resonance Imaging Methodology,” *European Journal of Nuclear Medicine and Molecular Imaging*, vol. 36, no. 1, pp. 30–41, 2009.

[5] R. Babaloo and E. Atalar, “Nonlinear droop compensation for current waveforms in MRI gradient systems,” *Magnetic Resonance in Medicine*, 2022.

[6] B. Zhang, K. Wang, and T. Jiang, “RF power design optimization in MRI system,” *Magnetic Resonance Letters*, vol. 1, no. 1, pp. 89–98, 2021.

[7] K. W. Fishbein, J. C. McGowan, and R. G. Spencer, “Hardware for Magnetic Resonance Imaging,” in *MR Imaging in White Matter Diseases of the Brain and Spinal Cord*, pp. 13–28, Springer, 2005.

[8] R. Frass-Kriegl, S. Hosseinnezhadian, M. Poirier-Quinot, E. Laistler, and J.-C. Ginefri, “Multi-loop radio frequency coil elements for magnetic resonance

imaging: theory, simulation, and experimental investigation," *Frontiers in Physics*, p. 237, 2020.

[9] B. Gruber, M. Froeling, T. Leiner, and D. W. Klomp, "RF coils: A practical guide for nonphysicists," *Journal of Magnetic Resonance Imaging*, vol. 48, no. 3, pp. 590–604, 2018.

[10] M. S. Aldemir, "Optimization of Coupled Class-E RF Power Amplifiers for a Transmit Array System in 1.5T MRI," Master's thesis, Bilkent Universitesi (Turkey), 2020.

[11] N. Gudino, Q. Duan, J. A. de Zwart, J. Murphy-Boesch, S. J. Dodd, H. Merkle, P. van Gelderen, and J. H. Duyn, "Optically controlled switch-mode current-source amplifiers for on-coil implementation in high-field parallel transmission," *Magnetic Resonance in Medicine*, vol. 76, no. 1, pp. 340–349, 2016.

[12] D. Hernandez and K.-N. Kim, "A review on the RF coil designs and trends for ultra high field magnetic resonance imaging," *Investigative Magnetic Resonance Imaging*, vol. 24, no. 3, pp. 95–122, 2020.

[13] J. H. Seo, H. Heo, B. Han, and S. Lee, "Comparison of birdcage and phase array coil using FDTD for the B_1 homogeneity in high field MRI," in *2007 29th Annual International Conference of the IEEE Engineering in Medicine and Biology Society*, pp. 3902–3905, IEEE, 2007.

[14] S. N. Williams, S. Allwood-Spiers, P. McElhinney, G. Paterson, J. Herrler, P. Liebig, A. M. Nagel, J. E. Foster, D. A. Porter, and S. Gunamony, "A nested eight-channel transmit array with open-face concept for human brain imaging at 7 tesla," *Frontiers in Physics*, vol. 9, 2021.

[15] Y. Zhu, "Parallel excitation with an array of transmit coils," *Magnetic Resonance in Medicine: An Official Journal of the International Society for Magnetic Resonance in Medicine*, vol. 51, no. 4, pp. 775–784, 2004.

[16] N. Gudino, J. A. de Zwart, Q. Duan, S. J. Dodd, J. Murphy-Boesch, P. van Gelderen, and J. H. Duyn, "Optically controlled on-coil amplifier

with RF monitoring feedback," *Magnetic Resonance in Medicine*, vol. 79, no. 5, pp. 2833–2841, 2018.

[17] U. Katscher and P. Börnert, "Parallel RF transmission in MRI," *NMR in Biomedicine: An International Journal Devoted to the Development and Application of Magnetic Resonance In vivo*, vol. 19, no. 3, pp. 393–400, 2006.

[18] K. Setsompop, L. L. Wald, V. Alagappan, B. Gagoski, F. Hebrank, U. Fontius, F. Schmitt, and E. Adalsteinsson, "Parallel RF transmission with eight channels at 3 tesla," *Magnetic Resonance in Medicine: An Official Journal of the International Society for Magnetic Resonance in Medicine*, vol. 56, no. 5, pp. 1163–1171, 2006.

[19] G. Adriany, E. J. Auerbach, C. J. Snyder, A. Gözübüyük, S. Moeller, J. Ritter, P.-F. Van de Moortele, T. Vaughan, and K. Uğurbil, "A 32-channel lattice transmission line array for parallel transmit and receive MRI at 7 tesla," *Magnetic Resonance in Medicine: An Official Journal of the International Society for Magnetic Resonance in Medicine*, vol. 63, no. 6, pp. 1478–1485, 2010.

[20] E. Kazemivalipour, A. Sadeghi-Tarakameh, and E. Atalar, "Eigenmode analysis of the scattering matrix for the design of MRI transmit array coils," *Magnetic Resonance in Medicine*, vol. 85, no. 3, pp. 1727–1741, 2021.

[21] N. Gudino, J. A. Heilman, M. J. Riffe, O. Heid, M. Vester, and M. A. Griswold, "On-coil multiple channel transmit system based on class-D amplification and pre-amplification with current amplitude feedback," *Magnetic Resonance in Medicine*, vol. 70, no. 1, pp. 276–289, 2013.

[22] W. Lee, E. Boskamp, T. Grist, and K. Kurpad, "Radiofrequency current source (RFCS) drive and decoupling technique for parallel transmit arrays using a high-power metal oxide semiconductor field-effect transistor (MOSFET)," *Magnetic Resonance in Medicine: An Official Journal of the International Society for Magnetic Resonance in Medicine*, vol. 62, no. 1, pp. 218–228, 2009.

[23] M. G. Zanchi, P. Stang, A. Kerr, J. M. Pauly, and G. C. Scott, "Frequency-offset Cartesian feedback for MRI power amplifier linearization," *IEEE Transactions on Medical Imaging*, vol. 30, no. 2, pp. 512–522, 2010.

[24] J. Heilman, M. Riffe, O. Heid, and M. Griswold, "High power, high efficiency on-coil current-mode amplifier for parallel transmission arrays," *Proceedings of the 15th ISMRM*, 2007.

[25] N. Gudino, J. A. de Zwart, and J. H. Duyn, "Eight-channel parallel transmit-receive system for 7 T MRI with optically controlled and monitored on-coil current-mode RF amplifiers," *Magnetic Resonance in Medicine*, vol. 84, no. 6, pp. 3494–3501, 2020.

[26] A. Kiri, K. Ohara, Y. Tomita, S. Shukuri, T. Yasukouchi, and T. Suetsugu, "Class-D and class-E selectable power amplifier," in *INTELEC 2009-31st International Telecommunications Energy Conference*, pp. 1–4, IEEE, 2009.

[27] N. O. Sokal and A. D. Sokal, "Class-E a new class of high-efficiency tuned single-ended switching power amplifiers," *IEEE Journal of Solid-State Circuits*, vol. 10, no. 3, pp. 168–176, 1975.

[28] R. Poni, "A Digitally Controlled Class-E Amplifier for MRI," Master's thesis, Bilkent Universitesi (Turkey), 2016.

[29] F. Zahra, "Highly efficient 300 W modified class-E RF amplifiers for 64 MHz transmit array system," Master's thesis, Bilkent Universitesi (Turkey), 2017.

[30] B. N. Ashfaq, "A gate modulated digitally controlled modified class-E amplifier for on-coil application in MRI," Master's thesis, Bilkent Universitesi (Turkey), 2018.

[31] A. Erkam Arslan, "A 600W On-coil Class-E RF Power Amplifier Array with Dynamic Phase Control for 3T MRI," Master's thesis, Bilkent Universitesi (Turkey), 2022.

[32] M. Acar, A. J. Annema, and B. Nauta, "Analytical design equations for class-E power amplifiers with finite DC-feed inductance and switch on-resistance,"

in *2007 IEEE International Symposium on Circuits and Systems*, pp. 2818–2821, IEEE, 2007.

[33] F. H. Raab and N. O. Sokal, "Transistor power losses in the class-E tuned power amplifier," *IEEE Journal of Solid-State Circuits*, vol. 13, no. 6, pp. 912–914, 1978.

[34] C. L. Phillips, H. T. Nagle, and A. Chakrabortty, *Digital control system analysis and design*, vol. 2. Prentice Hall Englewood Cliffs, NJ, 1990.

[35] K. Ogata *et al.*, *Modern control engineering*, vol. 5. Prentice Hall Upper Saddle River, NJ, 2010.

[36] K. J. Åström and B. Wittenmark, *Computer-controlled systems: theory and design.* Courier Corporation, 2013.

[37] A. Bräckle, L. Rathgeber, F. Siegert, S. Heck, and M. Berroth, "Power supply modulation for RF applications," in *2012 15th International Power Electronics and Motion Control Conference (EPE/PEMC)*, pp. LS8d–3, IEEE, 2012.

[38] A. B. Jusoh, M. H. B. Saiful, and T. Sutikno, "DC bus stabilization using passive damping network in distributed power system with constant power load," *TELKOMNIKA (Telecommunication Computing Electronics and Control)*, vol. 17, no. 1, pp. 425–437, 2019.